frontiers | Frontiers in Earth Science

TYPE Original Research
PUBLISHED 25 July 2022
DOI 10.3389/feart.2022.967003



OPEN ACCESS

EDITED BY
Zhuang Li,
China University of Petroleum, China

REVIEWED BY
Xisheng Xu,
Nanjing University, China
Shaowei Zhao,
Chang'an University, China

*CORRESPONDENCE
Jiao-Long Zhao,
jlz@lzu.edu.cn

SPECIALTY SECTION
This article was submitted to Petrology, a section of the journal Frontiers in Earth Science

RECEIVED 12 June 2022
ACCEPTED 04 July 2022
PUBLISHED 25 July 2022

CITATION
Zhao J-L, Chen W-F, Wang J-R, Tang Q-Y, Wang E-T and Fu Y-Q (2022), Petrogenesis of early–middle paleozoic granitoids in the qilianblock, northwest China: Insight into the transition from adakitic to non-adakitic magmatism in a post-collisional extensional setting. *Front. Earth Sci.* 10:967003. doi: 10.3389/feart.2022.967003



# Petrogenesis of early–middle paleozoic granitoids in the qilianblock, northwest China: Insight into the transition from adakitic to non-adakitic magmatism in a post-collisional extensional setting

Jiao-Long Zhao*, Wan-Feng Chen, Jin-Rong Wang, Qing-Yan Tang, Er-Teng Wang and Yi-Qiao Fu

Key Laboratory of Mineral Resources in Western China (Gansu Province), School of Earth Sciences, Lanzhou University, Lanzhou, China

To better understand geodynamic implications for the transition from adakitic to non-adakitic magmatism in a continental collision setting, an integrated study including zircon U–Pb ages and whole-rock geochemistry was performed for the Gahai and Erhai granitoid intrusions within the Qilian Block. The ca. 450–428 Ma Gahai biotite granite and Erhai muscovite-bearing granite are peraluminous S-type granites with adakitic geochemical characteristics, and have low Mg# (41.2–31.7) and $\varepsilon_{Nd}(t)$ (–10.8 to –6.5) values with two–stage Nd model ages of 2.05–1.72 Ga, implying their derivation almost entirely from an ancient crustal source under a thickened lower crust condition. The geochemical characteristics of the granites indicate that the Gahai and Erhai S-type granites were derived from partial melting of meta-greywacke and meta-pelite sources, respectively. In comparison, the ca. 415 Ma Gahai granodiorite belongs to metaluminous I-type granitoid and has low Sr/Y ratios as well as high Y and heavy rare Earth element (REE) concentrations, with nearly flat heavy REE patterns, implying a shallow source region. The granodiorites were most likely generated by partial melting of a K-rich basaltic magma source, with some contributions from mantle-derived melts. Synthesized data from this and previous studies suggest that the ca. 450–415 Ma Gahai and Erhai granitoids within the Qilian Block were generated in a post-collisional extensional regime triggered by the break-off of the northward subducting South Qilian Ocean slab beneath the Qilian Block. The geochemical transition from adakitic to non-adakitic intermediate-acidic magmas indicated that the thickened continental crust of the Qilian Block had experienced significant extension and thinning after ca. 420 Ma.

KEYWORDS

**early-middle paleozoic magmatism, adakitic S-type granite, non-adakitic I-type granodiorite, slab break-off, qilian block**

# 1 Introduction

Orogenic evolution generally comprises a period of crustal thickening followed by extension and thinning of the previously thickened crust (Vanderhaeghe and Teyssier, 2001; Xu et al., 2013). Adakitic magmas in continental settings are regarded as good indicators of crustal thickening as they have unique geochemical characteristics (Chung et al., 2003; Hu et al., 2017). The transition from adakitic rocks to non-adakitic rocks at convergent margins is usually attributed to a change in tectonic regime, although the geodynamic mechanism responsible for this geochemical transition remains controversial. Some studies have suggested that the change in composition from adakitic rocks to non-adakitic rocks in an oceanic subduction zone reflects a tectonic switch from an advancing subduction compressive regime to a retreating subduction extensional regime (Qiu et al., 2014; Liu et al., 2016; Xia Y. et al., 2016). However, most researchers have attributed this geochemical transition in a continental collision setting to continuous crustal thinning controlled by a post-collisional extensional regime, as a result of delamination of a previously thickened crust and/or the break-off of the subducted oceanic slab (Xiao et al., 2007; Xu et al., 2013; Gao et al., 2014; Yang et al., 2016). Nevertheless, some studies also have proposed that the occurrence of non-adakitic granites after adakitic granites marks the transition from a compressional tectonic regime to an extensional one (Ma et al., 2004; Zhao et al., 2014; Zhang et al., 2018). According to any of the geodynamic models, the geochemical transition of the magmas from adakitic to non-adakitic calc-alkaline in collisional orogenic belts provides an opportunity to investigate the tectonic and geodynamic processes of an area.

The Qilian orogenic belt situated in the northeastern margin of the Tibetan Plateau is a typical accretionary orogenic belt (Figure 1A). The progressive subduction and final closure of a branch of Proto-Tethys Ocean in the early Paleozoic (480–400 Ma, Li et al., 2018) gave rise to the accretion and amalgamation of the Qilian Block and the neighboring microcontinents such as Qaidam and Alxa Blocks at the eastern end of the northern margin of Gondwana and eventually assembled the Qilian orogenic belt, which is composed of the North Qaidam ultrahigh-pressure metamorphic (UHPM) belt, Qilian Block, and North Qilian orogenic belt from south to north (Figure 1A; Song et al., 2013; Li et al., 2018; Yao et al., 2021). Voluminous early Paleozoic magmatic rocks, typically consisting of granitoids, with minor amounts of mafic rocks, are widely distributed within the Qilian orogenic belt and have attracted much attention (Song et al., 2014; Huang et al., 2016; Tung et al., 2016; Xia et al., 2016; Li et al., 2017; Wang et al., 2019). These igneous rocks are thought to have been produced in response to ocean plate subduction and subsequent collisional orogenic processes. However, the focus of most previous research in this area has been the early Paleozoic granitoids and ophiolites, with little attention paid to the early Devonian granitoids in the Qilian orogenic belt (Tung et al., 2016; Xia et al., 2016; Yang et al.,

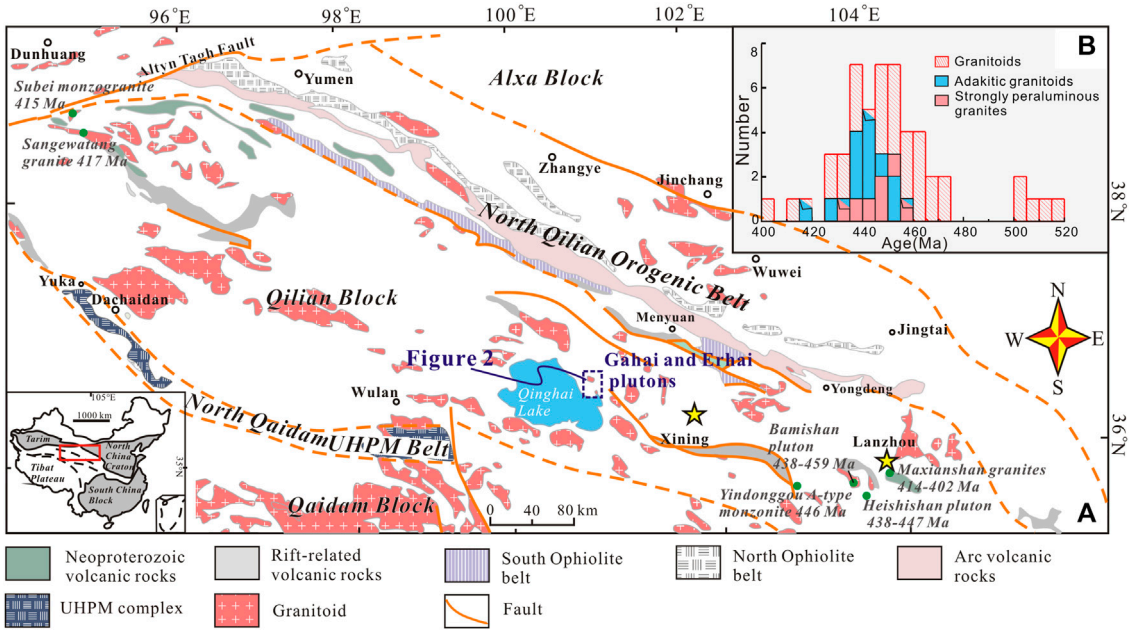


FIGURE 1
**(A)** Geological sketch map of the Qilian orogenic belt showing distributions of early–middle Paleozoic magmatic rocks and their ages (modified from Xia et al., 2016). Zircon U–Pb ages in previous studies are from Cui et al. (2019), Wang et al. (2017), Tung et al. (2016) and Yang et al. (2015) **(B)** Frequency of zircon U–Pb ages for the magmatic rocks from the eastern Qilian Block (modified from Zhao et al., 2021).

2021). This has hampered our understanding of the geodynamics and tectonic evolution of the whole Qilian orogenic belt. The Qilian Block, lying between the critical junction of the North Qilian Orogenic belt and the North Qaidam ultrahigh-pressure metamorphic belt (Figure 1), was expected to provide a good record of the tectonic processes that formed the Qilian orogenic belt. Magmatic activities in the Qilian Block were well developed during the late Paleozoic to early Devonian (Tung et al., 2016; Xia et al., 2016; Yang et al., 2021; Zhao et al., 2021), and thus provide an excellent target for tracing the tectonic evolution of the Qilian Block, and to investigate the accretionary history of the Qilian orogenic belt. More importantly, many studies have suggested that the early Paleozoic granitoids in the Qilian Block, mostly S-type and I-type granitoids, usually show adakitic geochemical characteristics (Tung et al., 2016; Xia et al., 2016; Cui et al., 2019; Yang et al., 2021; Zhao et al., 2021). In contrast, the early Devonian granitoids, which were sporadically emplaced in the Qilian Block, tended to have non-adakitic high-K calc-alkaline features (Tung et al., 2016; Wang et al., 2017). Unfortunately, little attention has been paid to this geochemical transition, with the geodynamic mechanism responsible for this transition still unclear.

In this study, we carried out geochronological, elemental, and isotopic analyses on the Silurian adakitic S-type granites and early Devonian non-adakitic I-type granodiorite from the Gahai and Erhai plutons in the Qilian Block (Figure 1). These new data combined with previously published data, will improve our understanding of the spatiotemporal distribution of the early–middle Paleozoic granitoids in the Qilian Block. It could also provide insight into the petrogenesis and sources of magma for the granitoids. This would in turn facilitate a greater understanding of the tectonic history of the Qilian Block and the Qilian orogenic belt.

## 2 Geological setting

The Qilian orogenic belt is a component of the Central China Orogen (namely, the Sulu–Dabie–Qinling–Qilian–Altun–Kunlun orogenic systems) that is generally regarded as the northernmost orogenic collage of the Proto-Tethys domain (Song et al., 2013; Li et al., 2018; Yao et al., 2021; Yu et al., 2021). It lies between the Alxa Block to the north and the Qaidam Block–West Qinling orogenic belt to the south and is offset to the northwest by the sinistral Altyn Tagh fault (Figure 1). The North Qilian Orogenic belt is composed of the northern back-arc ophiolite belt, the middle arc magmatic belt, and the southern ophiolite belt (Figure 1). It is characterized by NW-trending prolonged granitoid intrusions, low-T/high-P eclogites, and blueschists, which are thought to be a product of northwards subduction of the North Qilian ocean (as a branch of the Proto-Tethys Ocean) and subsequent continental collision during the early Paleozoic (Xia et al., 2016; Wang et al., 2019; Yu et al., 2021). The North Qaidam ultrahigh-pressure metamorphic belt extends discontinuously for ~400 km, and formed during a collisional orogenic event. It is characterized by ultrahigh-pressure (UHP) metamorphic pelitic/granitic gneisses intercalated with minor eclogites and garnet peridotite blocks (Xia et al., 2016; Yu et al., 2021). These clogite and garnet peridotite blocks gave peak UHP metamorphic ages of 440–420 Ma (Zhou et al., 2021). The Qilian Block is predominantly composed of Precambrian basement and Neoproterozoic to Devonian intrusive rocks overlain unconformably by supracrustal Phanerozoic sedimentary sequences (Tung et al., 2013, 2016). The Precambrian crystalline basement rocks consist of significantly deformed gneisses, migmatites, slates, phyllites, schists, marbles, quartzites, and medium to high-grade amphibolites (Zhang et al., 2006; Xia et al., 2016; Li et al., 2020). As shown in Figure 1B, the early–middle Paleozoic magmatic rocks are widespread in the Qilian Block, with a major peak between 455 and 435 Ma. They are typically composed of high-K calc-alkaline S-type and I-type granitoids, with minor amounts of A-type granitoids and mafic rocks (Tung et al., 2016; Wang et al., 2017; Cui et al., 2019; Yang et al., 2021). They have been interpreted as products in response to varying stages of an orogenic cycle, from oceanic subduction, continental collision to orogenic collapse (Tung et al., 2016; Yang et al., 2021).

## 3 Petrography

The Gahai and Erhai granitoid plutons, each with an exposed area of less than 30 $km^2$, are located in Haiyan County, Qinghai Province. They occur as an elongated shape, with the long axis extending NW–SE, parallel to the North Qaidam ultra-high pressure metamorphic belt. Both of the plutons intruded into the Precambrian Huangyuan Group (Figure 2). The Gahai pluton is composed of granodiorite and biotite granite, with the latter situated in the central part of the pluton (Figure 2). The biotite granites are fine-grained to medium-grained, with granitic textures, and composed of quartz (20–35 vol%), plagioclase (15–20 vol%), alkali-feldspar (40–45 vol%), and biotite (~6 vol%) (Figures 3A,B), with minor amounts of apatite and zircon. The granodiorite is medium to coarse-grained, has a porphyritic texture, with ~5 vol% phenocrysts (Figures 3A,C). The groundmass is composed mainly of quartz, plagioclase, biotite, alkali-feldspar, and amphibole, with accessory apatite, titanite, zircon and Ti-Fe oxides (Figure 3D). The phenocrysts are dominated by alkali-feldspar and quartz. The Erhai pluton consists mainly of muscovite-bearing granite. The muscovite-bearing granites have a medium-grained to coarse-grained granitic texture, and consist of alkali-feldspar (45–50 vol%), quartz (20–25 vol%), plagioclase (15–20 vol%), muscovite (~5 vol%) and biotite (<5 vol%), with accessory zircon and Ti-Fe oxides (Figures 3E,F). The quartz grains from the Gahai

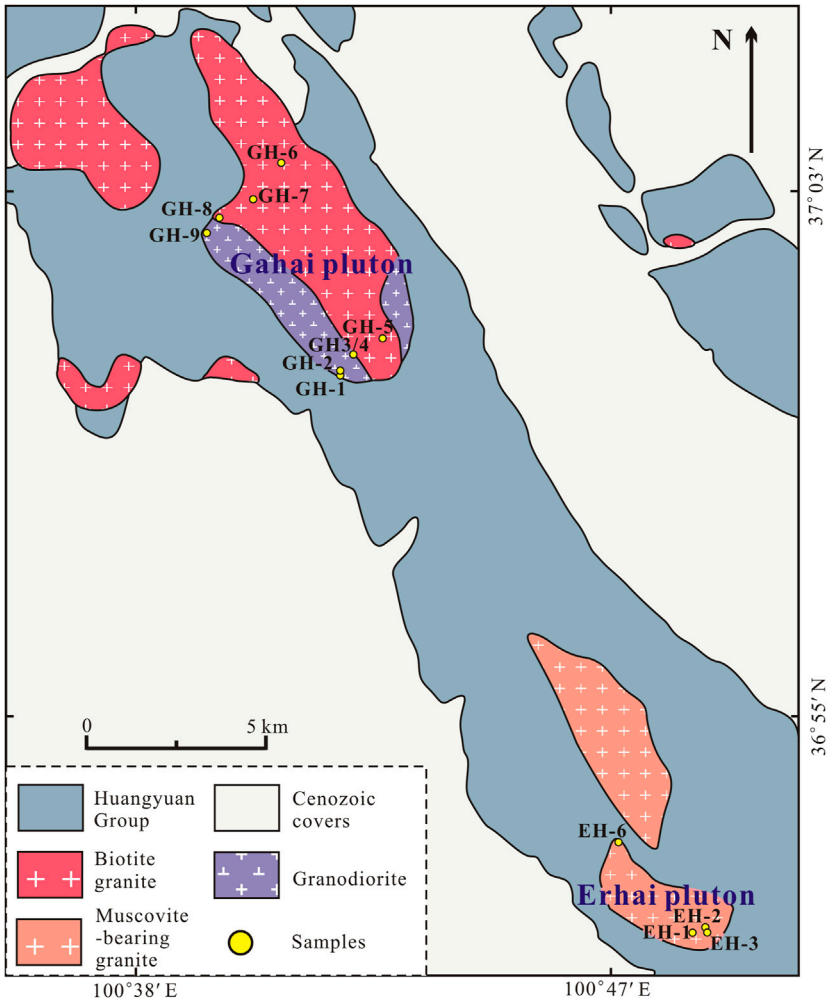


FIGURE 2
Simplified geological map of the Gahai and Erhai granitoid intrusions in the Haiyan region, northwest China (modified after 1: 200, 000 geological map of the Haiyan area) showing sample localities.

biotite granite and Erhai muscovite-bearing granite exhibit clear undulatory extinction. Moreover, both Gahai biotite granite and the Erhai muscovite-bearing granite are characterized by the common occurrence of granophyric textures, and mafic microgranular enclaves (MME) are rarely observed (Figure 3). In contrast, MMEs with spheroidal to ellipsoid–ovoid shapes are scattered throughout the Gahai granodiorite, with typical sizes 2–15 cm in diameter (Figure 3C).

# 4 Analytical methods

Samples weighing about 5 kg each were collected by the authors during fieldwork in 2017. Details of the sampling locations are presented in Figure 2. Selected fresh whole-rock samples were crushed and powdered to 200 mesh in an agate ring mill for whole-rock geochemical analyses. Zircon grains were separated by standard density and magnetic techniques. The selection of individual zircon grains was made using a binocular microscope. Representative zircon grains were mounted in epoxy resin and subsequently polished to expose the interior of the grains.

## 4.1 Zircon U–Pb dating

Three samples (i.e., GH-1 for the Gahai granodiorite, GH-8 for the Gahai biotite granite, and EH-1 for the Erhai muscovite-bearing granite) in this study were selected for zircon U–Pb dating. Cathodoluminescence images (CL) of zircons in the plutons were obtained using a Gatan Mini CL detector attached to a JSM-6510 scanning electron microscope at the Key Laboratory of Mineral Resources, Lanzhou University, Lanzhou, China.

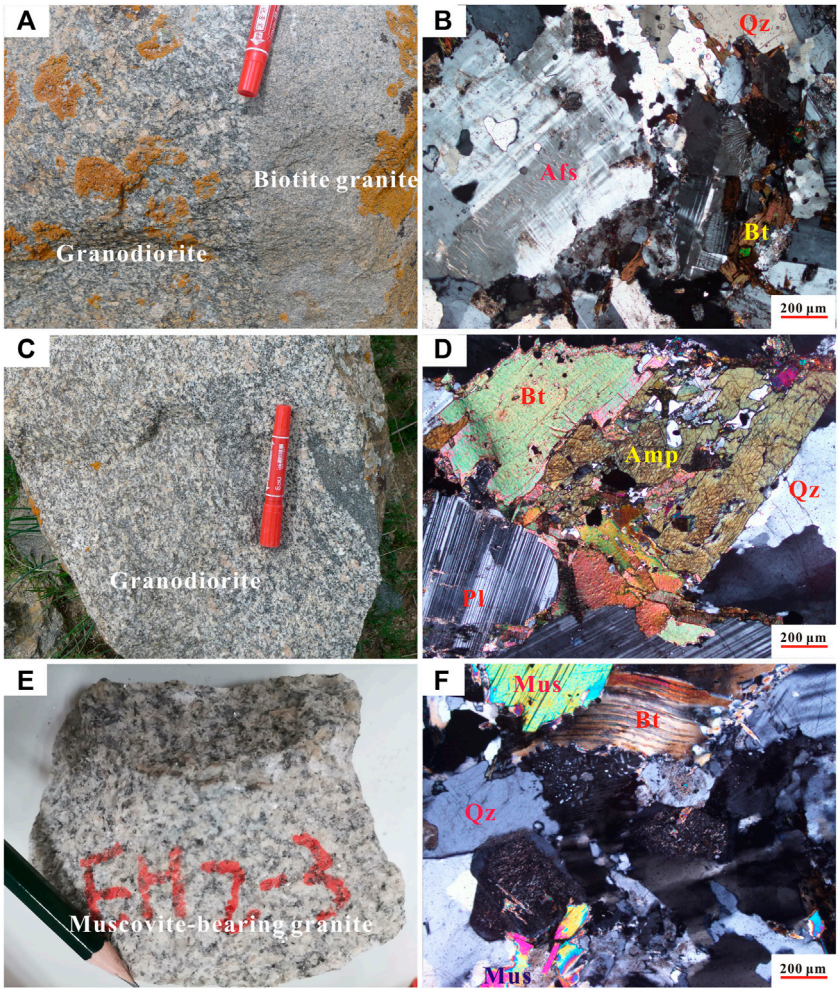


FIGURE 3
Macroscopic and thin section images of rocks from the Gahai and Erhai plutons **(A)** Sharp contact between the granodiorite and biotite granite within the Gahai pluton; **(B)** Gahai biotite granite (crossed nicols); **(C)** Gahai granodiorite bearing microgranular mafic enclaves; **(D)** Gahai granodiorite (crossed nicols); **(E)** Erhai muscovite-bearing granite; **(F)** Erhai muscovite-bearing granite with granophyric texture (crossed nicols). Mineral abbreviation: Qtz, quartz; Afs, alkali-feldspar; Pl, plagioclase; Bt, biotite; *Mus*, muscovite; Amp, amphibole.

Zircon U–Pb isotopic analyses were carried out using an Agilent 7500a inductively coupled plasma–mass spectrometer (ICP–MS) coupled to a New Wave Research 213 nm laser ablation system at the State Key Laboratory for Mineral Deposits Research (SKLMDR), Nanjing University. Analyses were carried out using a beam diameter of 32 μm, a repetition rate of 5 Hz, and an energy of 23.74–26.68 J/cm$^2$. A homogeneous standard zircon (GEMOC GJ-1) was used to correct the mass discrimination of the mass spectrometer and residual elemental fractionation. Zircon Mud Tank was used as an independent control for reproducibility and instrument stability. The raw ICP–MS U–Pb isotopic data were acquired using GLITTER 4.4, using the method for common Pb described by Andersen (2002). Isoplot 4.15 software was used for weighted-mean calculations and for plotting concordia diagrams.

## 4.2 Whole-rock major and trace element, and Sr–Nd isotope analyses

Whole-rock major element analyses were performed using a Thermo Scientific ARL 9900 X-ray fluorescence (XRF) spectrometer at SKLMDR. Mixtures of whole-rock powders (0.5 g) and $Li_2B_4O_7$ + $LiBO_2$ + LiBr (11 g) were made into glass discs and then analyzed by XRF. The analytical precision was estimated to be less than 10% for all major elements and less than 1% for the majority of elements. Trace element concentrations were measured using a Finnigan Element II ICP–MS at SKLMDR. Detailed analytical procedures followed Gao et al. (2003). The analytical precision was better than 10% for all trace elements, with the majority being better than 5%.

TABLE 1 LA–ICP–MS zircon U–Pb dating results of representative samples from the Gahai and Erhai plutons.

| Spot no. | Th/U | Isotopic ratios | | | | | | Ages (Ma) | | | |
|---|---|---|---|---|---|---|---|---|---|---|---|
| | | $^{207}Pb/^{206}Pb$ | | $^{207}Pb/^{235}U$ | | $^{206}Pb/^{238}U$ | | $^{207}Pb/^{235}U$ | | $^{206}Pb/^{238}U$ | |
| | | Ratio | ±1σ | Ratio | ±1σ | Ratio | ±1σ | Age | ±1σ | Age | ±1σ |
| Gahai granodiorite | | | | | | | | | | | |
| GH-1, coordinate: 37°00′12″N, 100°41′54″E | | | | | | | | | | | |
| GH1-01 | 1.33 | 0.05761 | 0.00116 | 0.53321 | 0.01074 | 0.06714 | 0.00085 | 434 | 7 | 419 | 5 |
| GH1-02 | 1.21 | 0.05473 | 0.00135 | 0.50579 | 0.01231 | 0.06704 | 0.00092 | 416 | 8 | 418 | 6 |
| GH1-03 | 0.75 | 0.06022 | 0.00159 | 0.55292 | 0.01478 | 0.06653 | 0.00107 | 447 | 10 | 415 | 6 |
| GH1-04 | 0.80 | 0.05854 | 0.00127 | 0.53676 | 0.01165 | 0.06651 | 0.00088 | 436 | 8 | 415 | 5 |
| GH1-05 | 0.97 | 0.05615 | 0.00140 | 0.51240 | 0.01255 | 0.06620 | 0.00089 | 420 | 8 | 413 | 5 |
| GH1-06 | 0.52 | 0.05800 | 0.00089 | 0.53011 | 0.00859 | 0.06629 | 0.00083 | 432 | 6 | 414 | 5 |
| GH1-07 | 0.74 | 0.06215 | 0.00126 | 0.56908 | 0.01201 | 0.06641 | 0.00093 | 457 | 8 | 414 | 6 |
| GH1-08 | 1.09 | 0.05490 | 0.00099 | 0.50500 | 0.00952 | 0.06672 | 0.00087 | 415 | 6 | 416 | 5 |
| GH1-09 | 1.02 | 0.05838 | 0.00206 | 0.53127 | 0.01822 | 0.06600 | 0.00103 | 433 | 12 | 412 | 6 |
| GH1-10 | 0.71 | 0.05493 | 0.00098 | 0.50310 | 0.00915 | 0.06643 | 0.00083 | 414 | 6 | 415 | 5 |
| GH1-11 | 1.32 | 0.05588 | 0.00101 | 0.51093 | 0.00949 | 0.06632 | 0.00084 | 419 | 6 | 414 | 5 |
| GH1-12 | 1.06 | 0.05553 | 0.00155 | 0.50846 | 0.01399 | 0.06641 | 0.00093 | 417 | 9 | 414 | 6 |
| GH1-13 | 0.83 | 0.05672 | 0.00121 | 0.51738 | 0.01127 | 0.06617 | 0.00089 | 423 | 8 | 413 | 5 |
| GH1-14 | 1.07 | 0.05540 | 0.00127 | 0.51129 | 0.01189 | 0.06694 | 0.00092 | 419 | 8 | 418 | 6 |
| GH1-15 | 1.09 | 0.05615 | 0.00129 | 0.51632 | 0.01195 | 0.06670 | 0.00093 | 423 | 8 | 416 | 6 |
| GH1-16 | 1.26 | 0.05789 | 0.00164 | 0.53109 | 0.01470 | 0.06654 | 0.00095 | 433 | 10 | 415 | 6 |
| Gahai biotite granite | | | | | | | | | | | |
| GH-8, coordinate: 37°02′35″N, 100°39′36″E | | | | | | | | | | | |
| GH8-01 | 0.63 | 0.06633 | 0.00502 | 0.66434 | 0.04944 | 0.07264 | 0.00100 | 517 | 30 | 452 | 6 |
| GH8-02 | 0.36 | 0.06740 | 0.00341 | 0.67003 | 0.03249 | 0.07210 | 0.00106 | 521 | 20 | 449 | 6 |
| GH8-03 | 0.39 | 0.08173 | 0.00719 | 0.79474 | 0.06869 | 0.07052 | 0.00116 | 594 | 39 | 439 | 7 |
| GH8-04 | 0.43 | 0.05958 | 0.00083 | 0.59907 | 0.00908 | 0.07292 | 0.00091 | 477 | 6 | 454 | 5 |
| GH8-05 | 0.51 | 0.06127 | 0.00110 | 0.61656 | 0.01138 | 0.07298 | 0.00093 | 488 | 7 | 454 | 6 |
| GH8-06 | 0.80 | 0.07529 | 0.00097 | 1.33343 | 0.01920 | 0.12844 | 0.00162 | 860 | 8 | 779 | 9 |
| GH8-07 | 1.05 | 0.06801 | 0.00119 | 1.04665 | 0.01948 | 0.11160 | 0.00154 | 727 | 10 | 682 | 9 |
| GH8-08 | 0.86 | 0.06322 | 0.00534 | 0.62611 | 0.05210 | 0.07183 | 0.00102 | 494 | 33 | 447 | 6 |
| GH8-09 | 0.43 | 0.06057 | 0.00086 | 0.60939 | 0.00945 | 0.07297 | 0.00093 | 483 | 6 | 454 | 6 |
| GH8-10 | 1.07 | 0.07264 | 0.00217 | 0.72879 | 0.02145 | 0.07278 | 0.00112 | 556 | 13 | 453 | 7 |
| GH8-11 | 1.44 | 0.06978 | 0.00120 | 1.26061 | 0.02256 | 0.13104 | 0.00169 | 828 | 10 | 794 | 10 |
| GH8-12 | 0.12 | 0.06058 | 0.00810 | 0.59402 | 0.07875 | 0.07112 | 0.00126 | 473 | 50 | 443 | 8 |
| GH8-13 | 0.20 | 0.06071 | 0.00093 | 0.60867 | 0.01004 | 0.07272 | 0.00094 | 483 | 6 | 453 | 6 |
| GH8-14 | 0.13 | 0.06345 | 0.00933 | 0.62648 | 0.09114 | 0.07161 | 0.00153 | 494 | 57 | 446 | 9 |
| Erhai muscovite-bearing granite | | | | | | | | | | | |
| EH-1, coordinate: 36°51′44″N, 100°48′34″E | | | | | | | | | | | |
| EH1-01 | 0.58 | 0.07111 | 0.00797 | 1.32257 | 0.14676 | 0.13489 | 0.00218 | 856 | 64 | 816 | 12 |
| EH1-02 | 1.23 | 0.05865 | 0.00118 | 0.55742 | 0.01147 | 0.06894 | 0.00094 | 450 | 7 | 430 | 6 |
| EH1-03 | 0.26 | 0.05902 | 0.00257 | 0.56288 | 0.02317 | 0.06917 | 0.00097 | 453 | 15 | 431 | 6 |
| EH1-04 | 1.08 | 0.06397 | 0.00112 | 0.60910 | 0.01084 | 0.06907 | 0.00087 | 483 | 7 | 431 | 5 |

(Continued on following page)

TABLE 1 (*Continued*) LA–ICP–MS zircon U–Pb dating results of representative samples from the Gahai and Erhai plutons.

| Spot no. | Th/U | Isotopic ratios | | | | | | Ages (Ma) | | | |
|---|---|---|---|---|---|---|---|---|---|---|---|
| | | $^{207}Pb/^{206}Pb$ | | $^{207}Pb/^{235}U$ | | $^{206}Pb/^{238}U$ | | $^{207}Pb/^{235}U$ | | $^{206}Pb/^{238}U$ | |
| | | Ratio | ±1σ | Ratio | ±1σ | Ratio | ±1σ | Age | ±1σ | Age | ±1σ |
| EH1-05 | 0.53 | 0.12346 | 0.00484 | 5.02529 | 0.18430 | 0.29522 | 0.00411 | 1824 | 31 | 1,668 | 20 |
| EH1-06 | 0.15 | 0.05836 | 0.00158 | 0.55379 | 0.01479 | 0.06883 | 0.00102 | 447 | 10 | 429 | 6 |
| EH1-07 | 0.15 | 0.05517 | 0.00130 | 0.51838 | 0.01053 | 0.06815 | 0.00081 | 424 | 7 | 425 | 5 |
| EH1-08 | 0.20 | 0.05399 | 0.00223 | 0.52863 | 0.02120 | 0.07104 | 0.00135 | 431 | 14 | 442 | 8 |
| EH1-09 | 3.58 | 0.08927 | 0.00235 | 2.16415 | 0.05538 | 0.17584 | 0.00262 | 1,170 | 18 | 1,044 | 14 |
| EH1-10 | 0.49 | 0.11510 | 0.00183 | 4.96136 | 0.08175 | 0.31267 | 0.00391 | 1813 | 14 | 1754 | 19 |
| EH1-11 | 0.37 | 0.06454 | 0.00126 | 1.09401 | 0.02244 | 0.12296 | 0.00176 | 750 | 11 | 748 | 10 |
| EH1-12 | 0.84 | 0.10993 | 0.00158 | 4.81577 | 0.07488 | 0.31776 | 0.00410 | 1788 | 13 | 1779 | 20 |
| EH1-13 | 0.14 | 0.06756 | 0.00123 | 0.64868 | 0.01279 | 0.06964 | 0.00104 | 508 | 8 | 434 | 6 |
| EH1-14 | 0.45 | 0.06471 | 0.00235 | 0.61278 | 0.02074 | 0.06868 | 0.00091 | 485 | 13 | 428 | 5 |
| EH1-15 | 1.28 | 0.06830 | 0.00100 | 1.18696 | 0.01970 | 0.12603 | 0.00174 | 795 | 9 | 765 | 10 |
| EH1-16 | 0.14 | 0.05728 | 0.00130 | 0.54986 | 0.01260 | 0.06967 | 0.00099 | 445 | 8 | 434 | 6 |
| EH1-17 | 1.01 | 0.05585 | 0.00085 | 0.53536 | 0.00880 | 0.06953 | 0.00090 | 435 | 6 | 433 | 5 |
| EH1-18 | 0.17 | 0.06862 | 0.00099 | 1.34368 | 0.02081 | 0.14205 | 0.00178 | 865 | 9 | 856 | 10 |
| EH1-19 | 0.14 | 0.05464 | 0.00423 | 0.50112 | 0.03821 | 0.06652 | 0.00091 | 412 | 26 | 415 | 5 |
| EH1-20 | 0.11 | 0.05730 | 0.00290 | 0.53376 | 0.02596 | 0.06756 | 0.00093 | 434 | 17 | 421 | 6 |
| EH1-21 | 0.22 | 0.06164 | 0.00287 | 0.57255 | 0.02558 | 0.06737 | 0.00087 | 460 | 17 | 420 | 5 |
| EH1-22 | 0.70 | 0.07901 | 0.00147 | 0.76071 | 0.01511 | 0.06983 | 0.00102 | 574 | 9 | 435 | 6 |

Whole-rock Sr–Nd isotopic compositions were determined at Tianjin Shangnuo Geological Technology Co. Ltd., Tianjin, China. Geological rock powder was decomposed using high-pressure polytetrafluoroethylene bombs. Strontium and Nd were all purified from the same digestion solution using two steps column chemistry: The first exchange column combined with BioRad AG50W × 8 and Sr Spec resin was used to separate Sr and REE from the sample matrix. Neodymium was separated from the other REE in the second column with a Ln Spec-coated Teflon powder. The Sr-bearing and Nd-bearing solutions were dried out and re-dissolved in 1.0 ml 2 wt% $HNO_3$. Small aliquots of each were analyzed using Agilent Technologies 7,700× quadrupole ICP–MS to determine the exact contents of Sr and Nd present. Diluted solutions (50 ppb Sr and 50 ppb Nd) were introduced into Nu Instruments Nu Plasma II multi-collector ICP-MS using Teledyne Cetac Technologies Aridus II desolvating nebulizer system.

Raw data of isotopic ratios were corrected for mass fractionation by normalizing to $^{86}Sr/^{88}Sr$ = 0.1194 for Sr and $^{146}Nd/^{144}Nd$ = 0.7219 for Nd. International isotopic standards (NIST SRM 987 for Sr and JNdi-1 for Nd) were periodically analyzed to correct instrumental drift. Geochemical reference materials, namely USGS AVG-2 and RGM-2, were used for quality control purposes.

# 5 Analytical results

## 5.1 Zircon U–Pb ages

Zircon CL images and LA–ICP–MS zircon U–Pb dating results for three granite samples from the two plutons are listed in Table 1 and shown in Figure 4. The zircon grains extracted from the Gahai biotite granite (GH-8) sample have lengths of 80–150 μm and length/width ratios of 1:1 to 2:1. In contrast, zircon grains extracted from the Gahai granodiorite (GH-1) and Erhai muscovite-bearing granite (EH-1) samples are coarser, up to 100–250 μm in length, and have length to width ratios varying from 1:1 to 3:1. All the zircons are euhedral and subhedral, transparent, and pale yellow to colorless. They show regular oscillatory magmatic zoning in CL images (Figure 4) and mostly have relatively high Th/U ratios of 0.12–3.58, indicating a magmatic origin for the zircons (Corfu et al., 2003; Wu and Zheng, 2004).

### 5.1.1 Gahai pluton

Sixteen zircon analyses from sample GH-1 yielded concordant and consistent $^{206}Pb/^{238}U$ ages, ranging from 419 ± 5 Ma to 412 ± 6 Ma, with a weighted mean $^{206}Pb/^{238}U$ age of 415 ± 3 Ma [mean square weighted deviation

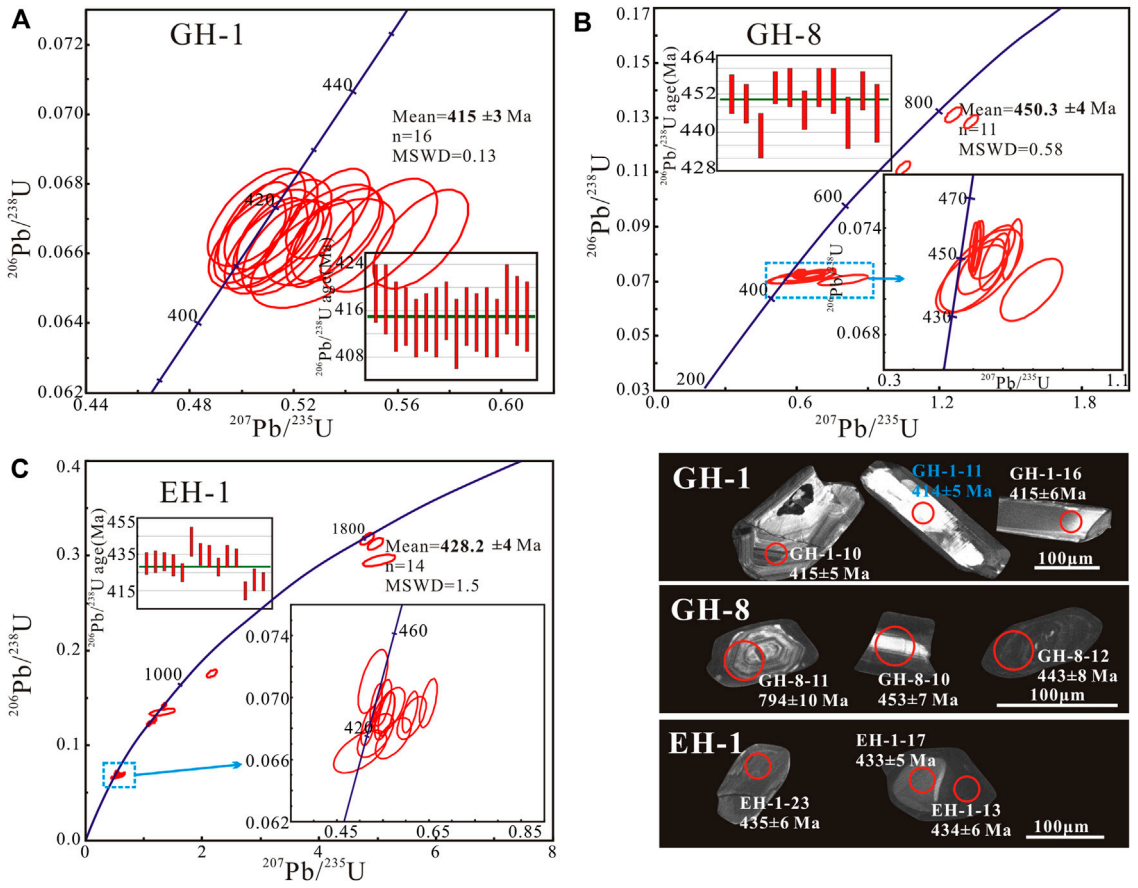


FIGURE 4
Representative CL images and U–Pb concordia diagrams for granodiorite **(A)** and biotite granite **(B)** within the Gahai pluton and muscovite-bearing granite **(C)** within the Erhai pluton.

(MSWD) = 0.13, Figure 4A]. Eleven of fourteen analyses from sample GH-8 have $^{206}Pb/^{238}U$ ages ranging from 454 ± 6 Ma to 439 ± 7 Ma, and yield a single age population with a weighted mean $^{206}Pb/^{238}U$ age of 450.3 ± 4 Ma (MSWD = 0.58, Figure 4B). Some zircons have a clear core–rim structure, with three analyses from the zircon cores giving older $^{206}Pb/^{238}U$ ages from 794 to 682 Ma. These age data indicate that the granodiorite and biotite granite within the Gahai pluton were emplaced at ca. 415 Ma and 450 Ma, respectively.

### 5.1.2 Erhai pluton

Fourteen analyses from sample EH-1 yielded concordant or nearly concordant $^{206}Pb/^{238}U$ ages ranging from 442 to 415 Ma. The weighted mean age of 428.2 ± 4 Ma (MSWD = 1.5, Figure 4C) was regarded as the crystallization age of the Erhai muscovite-bearing granite. Inherited zircon grains or xenocrysts in the Erhai muscovite-bearing granite had zircon core ages of 1779–748 Ma (Figure 4C).

## 5.2 Whole-rock major and trace element analyses

Whole-rock major and trace element data for granitoids from the Gahai and Erhai plutons have been presented in Table 2.

Three types of granitoids from the Gahai and Erhai plutons display moderate to high contents of total alkalis ($Na_2O + K_2O$ = 8.85–6.59 wt%) and all fall into the subalkaline series on a total alkalis vs. silica diagram (Figure 5A). The Gahai granodiorites have $SiO_2$ contents of 65.78–63.31 wt% and $K_2O$ contents of 3.99–2.86 wt%, with $K_2O/Na_2O$ ratios ranging from 1.2 to 0.8. In comparison, the Gahai biotite granite and Erhai muscovite-bearing granite generally have higher $SiO_2$, $K_2O$, but lower MgO concentrations, and higher $K_2O/Na_2O$ ratios (1.55–2.25). In the $K_2O$ vs. $SiO_2$ diagram, samples from the Gahai granodiorite plot within the high-K calc-alkaline series, whereas those for the Gahai biotite granite and Erhai muscovite-bearing granite belong to the shoshonite series (Figure 5B). All of the Gahai granodiorites are metaluminous

TABLE 2 Bulk rock major (wt%) and trace element (ppm) analyses of representative samples from the Gahai and Erhai plutons.

| Rock type | Gahai granodiorite | | | | Gahai biotite granite | | | | | Erhai muscovite-bearing granite | | | |
|---|---|---|---|---|---|---|---|---|---|---|---|---|---|
| Sample | GH-1 | GH-2 | GH-4 | GH-9 | GH-3 | GH-5 | GH-6 | GH-7 | GH-8 | EH-1 | EH-2 | EH-3 | EH-4 |
| $SiO_2$ | 63.90 | 64.40 | 65.78 | 63.31 | 69.74 | 73.23 | 72.65 | 72.52 | 71.86 | 73.19 | 75.52 | 72.49 | 74.38 |
| $TiO_2$ | 0.78 | 0.82 | 0.74 | 0.83 | 0.36 | 0.12 | 0.20 | 0.17 | 0.27 | 0.20 | 0.19 | 0.17 | 0.04 |
| $Al_2O_3$ | 16.12 | 15.80 | 15.91 | 16.64 | 14.77 | 13.43 | 13.94 | 13.54 | 14.10 | 14.02 | 13.84 | 13.33 | 14.01 |
| $Fe_2O_3^T$ | 5.17 | 5.19 | 4.70 | 5.43 | 2.32 | 1.11 | 1.50 | 1.40 | 1.68 | 1.55 | 1.47 | 1.37 | 0.76 |
| MnO | 0.07 | 0.07 | 0.07 | 0.08 | 0.04 | 0.03 | 0.03 | 0.03 | 0.03 | 0.03 | 0.04 | 0.03 | 0.07 |
| MgO | 1.57 | 1.57 | 1.64 | 1.78 | 0.82 | 0.26 | 0.41 | 0.33 | 0.51 | 0.39 | 0.34 | 0.35 | 0.16 |
| CaO | 3.73 | 3.54 | 3.35 | 4.11 | 1.92 | 1.02 | 1.37 | 1.21 | 1.23 | 0.85 | 0.77 | 0.97 | 0.66 |
| $Na_2O$ | 3.75 | 3.46 | 3.42 | 3.73 | 2.80 | 3.07 | 3.25 | 2.90 | 3.03 | 2.74 | 3.12 | 2.93 | 3.84 |
| $K_2O$ | 3.18 | 3.60 | 3.99 | 2.86 | 5.72 | 5.79 | 5.05 | 5.68 | 5.63 | 5.93 | 5.47 | 5.56 | 4.42 |
| $P_2O_5$ | 0.23 | 0.24 | 0.22 | 0.26 | 0.13 | 0.05 | 0.05 | 0.06 | 0.08 | 0.12 | 0.12 | 0.11 | 0.17 |
| LOI | 0.53 | 0.85 | 1.06 | 0.38 | 1.35 | 0.85 | 1.23 | 1.21 | 1.29 | 1.34 | 0.21 | 1.80 | 0.83 |
| Total | 99.03 | 99.53 | 100.86 | 99.42 | 99.96 | 98.95 | 99.68 | 99.05 | 99.71 | 100.37 | 101.09 | 99.11 | 99.35 |
| $K_2O/Na_2O$ | 0.85 | 1.04 | 1.17 | 0.77 | 2.04 | 1.89 | 1.55 | 1.96 | 1.86 | 2.16 | 1.75 | 1.90 | 1.15 |
| A/CNK | 0.98 | 0.98 | 0.99 | 0.99 | 1.03 | 1.02 | 1.05 | 1.03 | 1.06 | 1.12 | 1.11 | 1.06 | 1.14 |
| Mg# | 37.6 | 37.5 | 40.9 | 39.4 | 41.2 | 31.7 | 35.1 | 31.8 | 37.6 | 33.3 | 31.4 | 33.6 | 29.4 |
| DI | 71.8 | 72.8 | 74.3 | 69.1 | 85.3 | 92.7 | 89.7 | 91.1 | 89.8 | 91.6 | 92.5 | 92.0 | 94.0 |
| Sc | 16.98 | 15.56 | 13.16 | 18.47 | 5.61 | 2.78 | 4.32 | 3.61 | 2.61 | 2.87 | 3.72 | 2.82 | 3.99 |
| V | 79.28 | 82.37 | 82.35 | 91.73 | 37.83 | 7.34 | 17.53 | 11.58 | 20.07 | 15.69 | 13.94 | 11.24 | 2.87 |
| Cr | 18.63 | 19.97 | 24.91 | 22.33 | 34.62 | 8.39 | 7.81 | 8.22 | 8.17 | 18.91 | 16.23 | 6.64 | 3.60 |
| Co. | 12.02 | 12.63 | 11.43 | 13.10 | 5.17 | 1.08 | 2.33 | 1.52 | 2.52 | 1.91 | 1.81 | 1.74 | 0.41 |
| Ni | 12.45 | 13.64 | 14.37 | 14.20 | 15.27 | 2.81 | 3.54 | 4.30 | 3.35 | 3.72 | 3.57 | 3.18 | 1.38 |
| Ga | 21.60 | 21.21 | 19.76 | 20.34 | 18.75 | 15.99 | 17.27 | 17.19 | 16.21 | 16.56 | 17.71 | 16.44 | 16.39 |
| Cs | 7.82 | 5.65 | 5.99 | 5.82 | 6.29 | 9.24 | 13.85 | 9.26 | 5.15 | 20.11 | 19.02 | 19.13 | 25.47 |
| Rb | 107.6 | 115.0 | 119.2 | 98.8 | 208.4 | 279.2 | 242.6 | 275.8 | 227.1 | 343.3 | 343.3 | 333.2 | 283.5 |
| Ba | 1,375.1 | 1,542.5 | 1,291.3 | 2004.1 | 1,061.8 | 446.4 | 659.0 | 541.4 | 848.6 | 354.3 | 311.8 | 315.9 | 172.8 |
| Th | 13.12 | 17.69 | 12.56 | 6.45 | 30.66 | 26.48 | 23.47 | 35.00 | 37.33 | 30.07 | 28.05 | 26.15 | 6.73 |
| U | 1.89 | 2.44 | 1.60 | 2.56 | 2.07 | 2.64 | 2.38 | 2.03 | 2.38 | 2.07 | 2.30 | 1.94 | 2.83 |
| Ta | 0.68 | 0.74 | 0.85 | 2.04 | 1.08 | 1.96 | 1.69 | 1.69 | 1.30 | 2.44 | 2.98 | 2.21 | 2.89 |
| Nb | 13.75 | 13.62 | 14.53 | 21.03 | 13.77 | 13.77 | 13.42 | 16.38 | 13.22 | 19.20 | 20.41 | 17.90 | 14.38 |
| Pb | 17.95 | 20.29 | 23.89 | 15.30 | 39.45 | 43.66 | 44.29 | 37.93 | 42.74 | 33.77 | 32.00 | 32.17 | 32.65 |
| Sr | 379.9 | 359.2 | 344.9 | 398.5 | 216.0 | 91.60 | 126.0 | 114.3 | 148.7 | 80.21 | 79.09 | 77.87 | 47.39 |
| Zr | 330.1 | 334.9 | 240.7 | 293.8 | 219.0 | 94.99 | 126.9 | 135.4 | 183.7 | 117.1 | 108.9 | 105.3 | 41.25 |
| Hf | 8.99 | 9.07 | 6.83 | 8.20 | 6.55 | 3.66 | 4.33 | 4.79 | 5.93 | 4.31 | 4.06 | 3.95 | 2.52 |
| Y | 29.63 | 28.09 | 23.26 | 56.71 | 13.10 | 13.27 | 14.52 | 14.48 | 12.72 | 18.28 | 18.53 | 16.49 | 14.54 |
| La | 83.74 | 92.24 | 51.79 | 45.14 | 79.69 | 37.48 | 39.31 | 60.38 | 61.82 | 41.17 | 37.66 | 35.51 | 7.38 |
| Ce | 163.61 | 177.43 | 102.37 | 91.63 | 150.20 | 73.05 | 76.08 | 111.92 | 110.05 | 79.39 | 78.57 | 72.39 | 14.40 |
| Pr | 18.46 | 19.33 | 11.85 | 13.02 | 16.31 | 8.39 | 8.65 | 12.89 | 12.66 | 10.23 | 9.44 | 8.86 | 1.76 |
| Nd | 68.80 | 72.47 | 44.53 | 57.72 | 56.06 | 29.33 | 30.81 | 44.91 | 43.97 | 37.49 | 34.48 | 32.65 | 6.18 |
| Sm | 11.27 | 11.41 | 7.88 | 13.65 | 7.85 | 5.22 | 5.36 | 7.11 | 6.80 | 7.20 | 6.75 | 6.33 | 1.60 |
| Eu | 2.58 | 2.65 | 2.15 | 3.15 | 1.31 | 0.68 | 0.95 | 0.81 | 1.05 | 0.60 | 0.54 | 0.54 | 0.27 |
| Gd | 11.32 | 11.27 | 7.97 | 12.94 | 6.63 | 4.88 | 5.06 | 6.59 | 6.45 | 6.64 | 6.31 | 5.95 | 1.77 |
| Tb | 1.41 | 1.36 | 1.04 | 2.22 | 0.71 | 0.61 | 0.63 | 0.76 | 0.71 | 0.92 | 0.89 | 0.82 | 0.41 |
| Dy | 6.72 | 6.31 | 5.17 | 13.15 | 2.79 | 2.80 | 2.92 | 3.12 | 2.83 | 4.24 | 4.25 | 3.85 | 2.83 |
| Ho | 1.21 | 1.14 | 0.94 | 2.46 | 0.47 | 0.48 | 0.52 | 0.52 | 0.48 | 0.69 | 0.70 | 0.63 | 0.51 |
| Er | 3.51 | 3.35 | 2.69 | 6.73 | 1.45 | 1.44 | 1.57 | 1.60 | 1.49 | 1.93 | 1.95 | 1.75 | 1.51 |

(Continued on following page)

TABLE 2 (*Continued*) Bulk rock major (wt%) and trace element (ppm) analyses of representative samples from the Gahai and Erhai plutons.

| Rock type | Gahai granodiorite | | | | Gahai biotite granite | | | | | Erhai muscovite-bearing granite | | | |
|---|---|---|---|---|---|---|---|---|---|---|---|---|---|
| Sample | GH-1 | GH-2 | GH-4 | GH-9 | GH-3 | GH-5 | GH-6 | GH-7 | GH-8 | EH-1 | EH-2 | EH-3 | EH-4 |
| Tm | 0.44 | 0.42 | 0.33 | 0.86 | 0.17 | 0.19 | 0.21 | 0.20 | 0.18 | 0.24 | 0.24 | 0.22 | 0.24 |
| Yb | 2.76 | 2.62 | 2.02 | 5.06 | 1.15 | 1.22 | 1.39 | 1.30 | 1.17 | 1.48 | 1.52 | 1.38 | 1.60 |
| Lu | 0.40 | 0.39 | 0.30 | 0.67 | 0.18 | 0.19 | 0.21 | 0.20 | 0.18 | 0.22 | 0.22 | 0.20 | 0.23 |
| $t_{Zr}$ (°C) | 783.0 | 787.0 | 754.2 | 770.0 | 764.7 | 688.5 | 718.3 | 723.2 | 755.7 | 721.7 | 714.7 | 703.5 | 632.3 |

LOI, loss on ignition; A/CNK, $Al_2O_3/(CaO + Na_2O + K_2O)$ molar; Mg# = 100 × Mg/(Mg + Fe); DI, differentiation index; $Fe_2O_3^T$, total Fe expressed as $Fe_2O_3$; $t_{Zr}$(°C), zircon saturation temperature.

with A/CNK values [ = molar $Al_2O_3/(CaO + K_2O + Na_2O)$] of 0.99–0.98 (Figure 5C), and show higher Mg# values [ = 100 × Mg/(Mg + Fe), 40.9–37.5] than those of the pure crustal melts under continental crust P–T conditions (Figure 5D). In contrast, the Gahai biotite granite and Erhai muscovite-bearing granite have relatively high A/CNK values of 1.06–1.02 and 1.12–1.05, respectively, are peraluminous (Figure 5C), and show similar Mg# values (41.2–28.9) to pure crustal melts (Figure 5D). Three types of granitoids from the Gahai and Erhai plutons show low $10^4$Ga/Al ratios (2.54–2.17) and $FeO^T$/MgO ratios (4.38–2.55), and are free of Na-rich mafic minerals (e.g., arfvedsonite and aegirine). They are thus distinctly different from common A-type granites that have high $10^4$Ga/Al ratios (>2.6) and $FeO^T$/MgO ratios (>10) (Whalen et al., 1987; Eby, 1990). Their geochemical features, along with the presence of amphibole in the Gahai granodiorite, and common occurrence of typical peraluminous minerals (e.g., muscovite) in the Erhai granite, indicate that the metaluminous Gahai granodiorites could be classified as typical I-type granitoid, whereas the peraluminous Gahai biotite granite and Erhai muscovite-bearing granites could be classified as S-type granite (Chappell and White, 1974; Whalen et al., 1987). This inference was further supported by the presence of abundant inherited zircons in the Gahai biotite granite and Erhai muscovite-bearing granites, as S-type granites commonly contain abundant inherited zircons (Williams, 1998; Liu et al., 2020).

All of these granitoids are enriched in light rare Earth elements (REE) and large ion lithophile elements (LILE) such as Cs, Rb, and Th as well as are depleted in high field strength elements (HFSE) such as Nb, Ta, and Ti, with variable negative anomalies of Eu, Sr, and p (Figure 6B). Both the Gahai biotite granite and Erhai muscovite-bearing granite have relatively low heavy REEs (16.4–11.8 ppm) and Y (18.5–12.7 ppm) concentrations and high Gd/Yb ratios (5.78–2.59). In contrast, the Gahai granodiorites and the metasedimentary rocks of the Precambrian Huangyuan Group have relatively high heavy REEs (40.1–20.5 ppm) and Y (56.7–23.3 ppm) concentrations, but low Gd/Yb ratios (4.31–2.56) (Figure 6). On the La/Yb–Yb discrimination diagram, samples from the Gahai biotite granite and Erhai muscovite-bearing granite chiefly plot in the adakite field, while those of the Gahai granodiorite plot outside the non-adakitic and adakitic granitoid fields (Figure 7). Notably, the high La/Yb ratios of the Gahai granodiorite are due to significant enrichment with light REEs rather than depletion of heavy REEs (Figure 6A). Therefore, the Gahai granodiorite should be assigned to the non-adakitic high-K calc-alkaline I-type granite group, whereas the Gahai biotite granite and Erhai muscovite-bearing granite are adakitic S-type granites (Figure 7).

## 5.3 Whole-rock Sr–Nd isotopes

The whole-rock Sr–Nd isotope ratios for the studied granitic samples have been presented in Table 3 and illustrated in Figure 8. The Gahai granodiorites have relatively homogeneous initial $^{87}Sr/^{86}Sr$ ratios [$(^{87}Sr/^{86}Sr)_i$] of 0.7097–0.7098, and $\varepsilon_{Nd}(t)$ values of −6.12–−5.45, with two-stage Nd model ages ranging from 1.66 to 1.60 Ga. The Gahai biotite granites have similar Sr isotopic compositions to the coexisting granodiorite, having $(^{87}Sr/^{86}Sr)_i$ ratios of 0.7127–0.7100. They have negative $\varepsilon_{Nd}(t)$ values of −8.70–−6.53 and yield two-stage Nd model ages of 1.89–1.72 Ga. In contrast, the Erhai muscovite-bearing granite had lower $(^{87}Sr/^{86}Sr)_i$ ratios (0.7086–0.7076) and $\varepsilon_{Nd}(t)$ values (−10.84–−10.69) than the Gahai granodiorite and biotite granite (Figure 8B). The corresponding two-stage Nd model ages are strikingly older, ranging from 2.05 to 2.04 Ga. Notably, as samples from the Erhai pluton have very high $^{87}Rb/^{86}Sr$ (12.7–12.5) and Rb/Sr ratios (6.0–4.3), the $(^{87}Sr/^{86}Sr)_i$ values for these samples cannot be used for tracing the petrogenesis of the rocks due to the large uncertainties involved (Jahn et al., 2001; Jiang and Zhu, 2017).

# 6 Discussion

## 6.1 Petrogenesis of the I-type gahai granodiorite

The Gahai granodiorites have high $SiO_2$ and $K_2O$ contents, relatively high radiogenic Sr isotope ratios [$(^{87}Sr/^{86}Sr)_i$ =

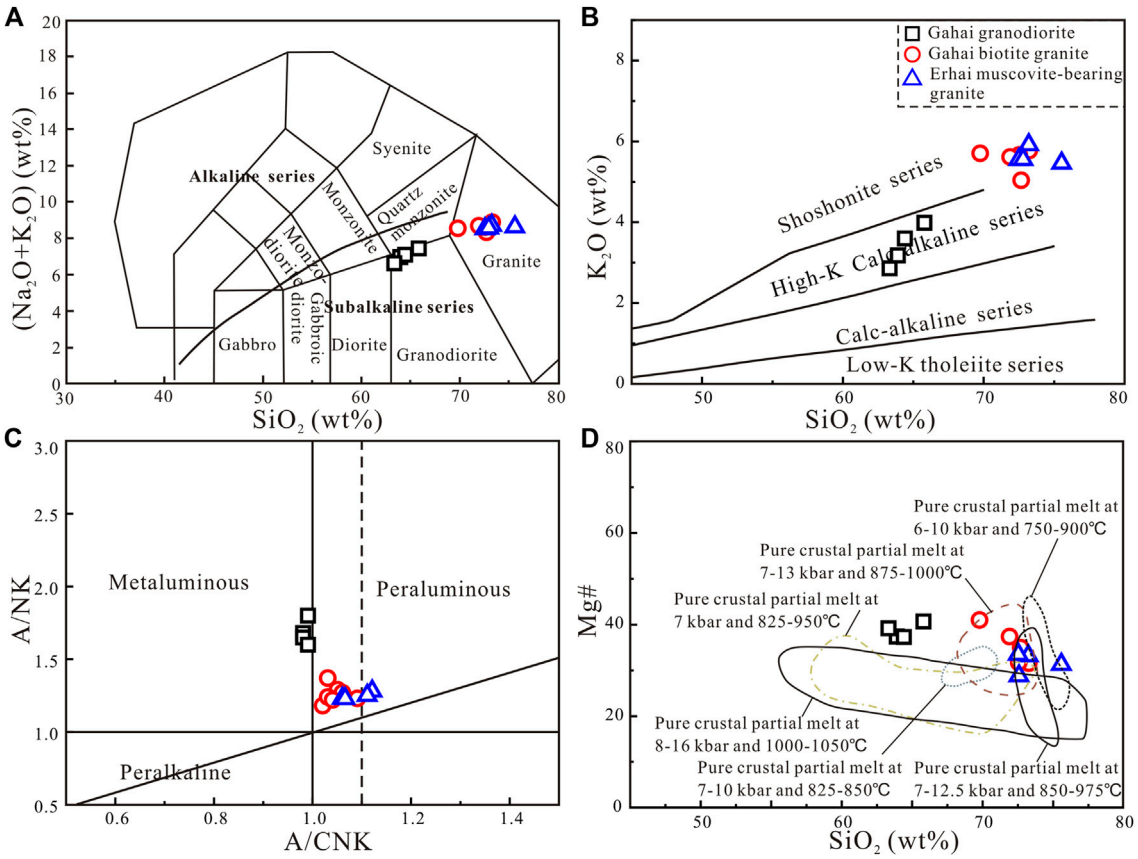


FIGURE 5
Geochemical classification of representative samples from the Gahai and Erhai plutons **(A)** Total alkali vs. silica diagram (Middlemost, 1994); with the thick solid line from (Irvine and Baragar, 1971); **(B)** $K_2O$ vs. $SiO_2$ diagram (Peccerillo and Taylor, 1976); **(C)** A/NK vs. A/CNK diagram (Chappell and White, 1974; Maniar and Piccoli, 1989); **(D)** Mg# vs. $SiO_2$ diagram (Jiang and Zhu, 2017).

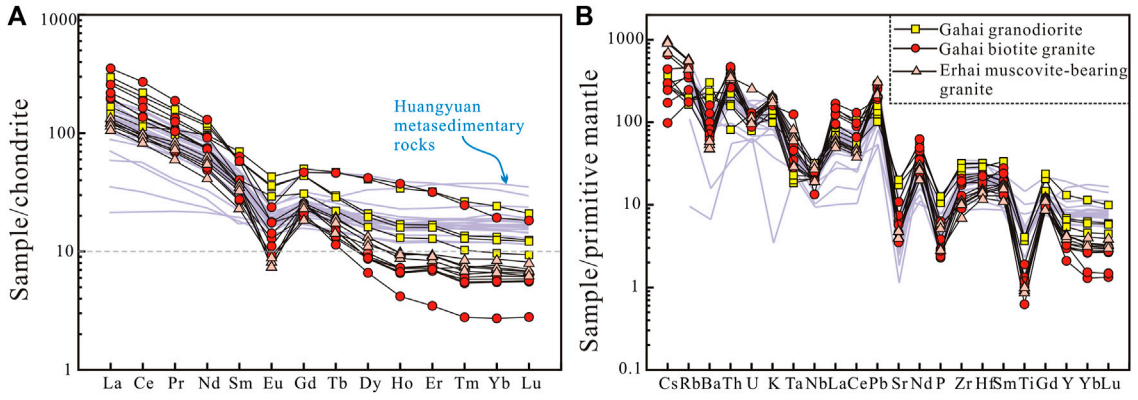


FIGURE 6
Chondrite-normalized REE patterns **(A)** and primitive-mantle-normalized trace element variation diagrams **(B)** of rocks from the Gahai and Erhai plutons. The data for chondrite and primitive mantle are from Boynton (1984) and McDonough and Sun (1995), respectively. The data for the Huangyuan Group metasedimentary rocks are from Li et al. (2020).

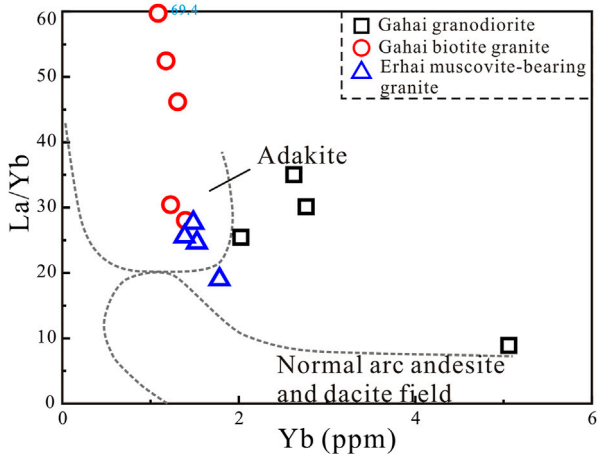


FIGURE 7
La/Yb vs. Yb diagram (Richards et al., 2012).

0.7097–0.7098], and negative $\varepsilon_{Nd}(t)$ (−6.12–−5.45) values, which would be consistent with a predominantly crustal source (Figure 8). Their Paleoproterozoic crustal model ages indicate that the magmatic sources may have been dominated by Paleoproterozoic crustal materials. More importantly, the Gahai and Erhai plutons have intruded the Huangyuan Group in the basement sequence of the Qilian Block, which provides ideal source materials for the generation of early-middle Paleozoic intermediate–felsic magmatic rocks in the Haiyan region. The Gahai granodiorites are metaluminous with A/CNK values of 0.99–0.98, and exhibit I-type affinities. They have high CaO + FeO + MgO + $TiO_2$ contents and molar CaO/(MgO + $FeO^T$) (0.66–0.60) values, and low molar $Al_2O_3$/(MgO + $FeO^T$) (1.57–1.46) and $K_2O/Na_2O$ (1.2–0.8) ratios. These compositions would be consistent with metaigneous source rock origins in the source discrimination diagram (Figure 9A), further suggesting their derivation from intermediate–mafic igneous source rocks (Chappell and White, 1974; Altherr et al., 2000). Experimental studies have shown that high-K calc-alkaline I-type magmas are usually derived from partial melting of medium-to high-K mafic to intermediate starting materials (Helz, 1976; Sisson et al., 2005). A K-rich intermediate–mafic protolith from the Huangyuan Group was the most likely candidate for crustal source materials.

Notably, the Gahai granodiorites have higher Mg# values than those derived solely by partial melting of crustal materials (Figure 5D). Moreover, normative hypersthene was present in all granodiorite samples. These traits reveal the contribution of mantle-derived melts during their generation (Bora and Kumar, 2015; Jiang and Zhu, 2017). This idea was supported by the presence of MMEs within the Gahai granodiorite. Some of the MMEs show irregular margins with K-feldspar xenocrysts (Figure 3C), indicating that the MMEs were present when the granodiorite intrusion was not yet completely solidified. In an age vs. $\varepsilon_{Nd}$ (t) diagram, samples from the granodiorite plot above the evolutionary trend defined by Neoproterozoic granitoids and metamorphic rocks from the Huangyuan Group (Figure 8A). Therefore, the Gahai granodiorites were most likely derived from partial melting of K-rich basic igneous rocks within the Huangyuan Group in the Qilian Block, with variable inputs of mantle-derived basic magma during their generation.

## 6.2 Petrogenesis of the adakitic S-type granites from the gahai and erhai plutons

Both the Gahai biotite granite and Erhai muscovite-bearing granite are apparently higher in silica than the later Gahai granodiorite. These two granites are peraluminous, with A/CNK values of 1.12–1.02, and show typical S-type geochemical characteristics, with the presence of muscovite in the Erhai granite. Moreover, they show enriched whole-rock Sr–Nd isotopic compositions, similar to the Neoproterozoic granitoids and the Precambrian metasedimentary rocks within the Huangyuan Group (Figure 8; Zhang et al., 2006; Tung et al., 2013), and hence consistent with a crustal origin. Taken together this indicates that the Precambrian metasedimentary rocks of the Huangyuan Group were the source material for the formation of the Gahai biotite granite and Erhai muscovite-bearing granite. This is supported by the frequent occurrence of Proterozoic zircon xenocrysts in the studied S-type granites (Figure 4).

The CaO/$Na_2O$ ratio of the melt was strongly influenced by the magma source regardless of temperature or pressure, and was considered to be useful means to determine source rock compositions, especially for distinguishing between pelite-derived melts and melts derived from graywackes, or igneous rocks (Sylvester, 1998; Jung and Pfänder, 2007). The Erhai muscovite-bearing granites had low CaO + FeO + MgO + $TiO_2$ contents and CaO/$Na_2O$ ratios (0.25–0.33), but high Rb/Ba (0.68–1.10) and Rb/Sr (2.86–4.34) ratios, which indicated a pelite-dominated origin (Figure 9; Sylvester, 1998). This view was reinforced by their high normative corundum contents (0.81–1.84), as melts sourced from metapelitic protolith are strongly peraluminous (Jung et al., 1998). However, the Gahai biotite granites have lower Rb/Ba (0.20–0.63), Rb/Sr (0.96–3.05) and A/CNK values, and higher CaO + FeO + MgO + $TiO_2$ contents and CaO/$Na_2O$ ratios (0.69–0.33) than the Erhai granites, further supporting the proposed derivation from metagraywacke source rocks (Figure 9; Sylvester, 1998). Notably, the Gahai biotite granite and Erhai muscovite-bearing granite have low Mg# values (41.2–28.9), similar to those formed solely by partial melting of crustal materials (Figure 5D, Jiang and Zhu, 2017). This, combined with the general scarcity of MMEs and magma mingling texture, indicates insignificant involvement of mantle-derived mafic melts during their generation.

TABLE 3 Whole-rock Rb–Sr and Sm–Nd isotopic data for the Gahai and Erhai granitoids.

| Sample no. | t (Ma) | Rb (ppm) | Sr (ppm) | $^{87}Rb/^{86}Sr$ | $^{87}Sr/^{86}Sr$ | $(^{87}Sr/^{86}Sr)_i$ | Sm (ppm) | Nd (ppm) | $^{147}Sm/^{144}Nd$ | $^{143}Nd/^{144}Nd$ | $\varepsilon_{Nd}(t)$ | $T_{DM2}$ (Ga) |
|---|---|---|---|---|---|---|---|---|---|---|---|---|
| Gahai granodiorite | | | | | | | | | | | | |
| GH-1 | 415 | 107.6 | 379.9 | 0.8200 | 0.714,533 ± 5 | 0.7097 | 11.3 | 68.8 | 0.0990 | 0.512,093 ± 4 | −5.45 | 1.60 |
| GH-9 | 415 | 98.8 | 398.5 | 0.7180 | 0.713,997 ±5 | 0.7098 | 13.7 | 57.7 | 0.1429 | 0.512,178 ± 6 | −6.12 | 1.66 |
| Gahai biotite granite | | | | | | | | | | | | |
| GH-5 | 450 | 279.2 | 91.6 | 8.8650 | 0.764,075 ± 7 | 0.7072 | 5.22 | 29.3 | 0.1075 | 0.511,930 ± 4 | −8.70 | 1.89 |
| GH-8 | 450 | 227.1 | 148.7 | 4.4332 | 0.738,390 ± 6 | 0.7100 | 6.80 | 44.0 | 0.0934 | 0.511,999 ± 3 | −6.53 | 1.72 |
| 87–1404c[a] | 450 | 148.5 | 70.5 | 6.1198 | 0.751,947 | 0.7127 | 11.4 | 78.0 | 0.0879 | 0.511,874 | −8.66 | 1.89 |
| 87–1404 h[a] | 450 | 105.6 | 70.0 | 4.3776 | 0.739,498 | 0.7114 | 9.73 | 61.8 | 0.0951 | 0.511,921 | −8.16 | 1.85 |
| Erhai muscovite-bearing granite | | | | | | | | | | | | |
| EH-1 | 428 | 343.3 | 80.2 | 12.4740 | 0.784,666 ± 6 | 0.7086 | 7.20 | 37.5 | 0.1160 | 0.511,864 ± 3 | −10.69 | 2.04 |
| EH-2 | 428 | 343.3 | 79.1 | 12.6505 | 0.784,670 ± 5 | 0.7076 | 6.75 | 34.5 | 0.1183 | 0.511,863 ± 4 | −10.84 | 2.05 |

$\varepsilon_{Nd}(t)$ values are calculated by granitoid ages and based on $^{147}Sm$ decay constant of $6.54 \times 10^{-12}$, the $^{143}Nd/^{144}Nd$ and $^{147}Sm/^{144}Nd$ ratios of chondrite and depleted mantle at present day are 0.512,630 and 0.1960, 0.513,151 and 0.2136, respectively (Miller and O'Nions, 1985). $T_{DM2}$ ages are calculated according to the two-stage model as presented by Wu et al. (2002).
[a]Data for the Gahai biotite granite are from Tung et al. (2016).

Taken together, we proposed that the Gahai biotite granite and Erhai muscovite-bearing granite were most likely generated by partial melting of metagraywacke and metapelite sources within the Precambrian Huangyuan Group, respectively, with negligible involvement of mantle-derived juvenile materials during their generation.

## 6.3 Petrogenetic model and geodynamic implications

Zircon U–Pb ages indicated that the S-type Gahai biotite granite and Erhai muscovite-bearing granite, with adakitic geochemical affinities, were emplaced from ca. 450–428 Ma. In contrast, the I-type Gahai granodiorites sequentially intruded into the Gahai biotite granite at ca. 415 Ma. Calculated zircon saturation temperatures for the Gahai and Erhai S-type granites ranged from 670.8–764.7°C, based on the equation of Watson and Harrison (1983), while the Gahai I-type granodiorites had temperatures ranging from 754.2 to 787.0°C. The $Al_2O_3/TiO_2$ ratio of a granite is considered as an indicator of temperature during partial melting (Sylvester, 1998; Jung and Pfänder, 2007). The fact that the Gahai I-type granodiorites have lower $Al_2O_3/TiO_2$ ratios (19.4–21.6) than those of the Gahai and Erhai S-type granite (40.9–128.7) further implies a higher magma temperature for the later Gahai I-type granodiorites. With respect to pressure, the relative depletion in HREE and Y resulted in high values of La/Yb and Gd/Yb for the Gahai and Erhai adakitic S-type granites (Figures 6, 7). This reflected high pressure conditions for their magma sources, where garnet could remain in a stable state in the residue. Moreover, Wang et al. (2012) proposed that both the plagioclase and alkali-feldspar were present as residual phases during the dehydration melting of mica-bearing metasedimentary rocks. The distinct negative Eu, Sr and Ba anomalies observed in the Gahai and Erhai S-type granites and significant enrichment in Rb suggest their generation by dehydration melting reactions of mica and the common existence of residual plagioclase and alkali feldspar in their magma source region, given that Rb and Ba are highly compatible in mica and alkali-feldspar, respectively and plagioclase is enriched in Eu and Sr (Harris and Inger, 1992; Rapp et al., 2003). Experiments indicate that garnet occurs as a residual mineral at pressures ≥12.5 kbar and the stability pressure of plagioclase is up to 15 kbar in the case of dehydration melting of metasedimentary rocks (Patiño Douce and Beard, 1995). These observations further suggest that the Gahai and Erhai S-type granites were derived from a deep source region with both garnet and plagioclase as the residual phases, corresponding to pressures of ca. 12.5–15 kbar. In comparison, the Gahai I-type granodiorites have high HREEs and Y concentrations with low Sm/Yb, point to a shallower source depth than those inferred for the generation of Gahai and Erhai adakitic S-type granites. It is suggested that the older Gahai and Erhai adakitic S-type granites were formed in low temperature–high pressure conditions, whereas the later Gahai I-type granodiorites were generated in high temperature–low pressure conditions. The occurrence and stability of abundant biotite and hornblende with accessory titanite in the Gahai I-type granodiorites, indicates the parental magma was rich in volatiles, especially water (Xirouchakis et al., 2001; Behrens and Gaillard, 2006). In comparison with the older Gahai and Erhai S-type granites, the Gahai granodiorites are less depleted in Eu and Sr, and

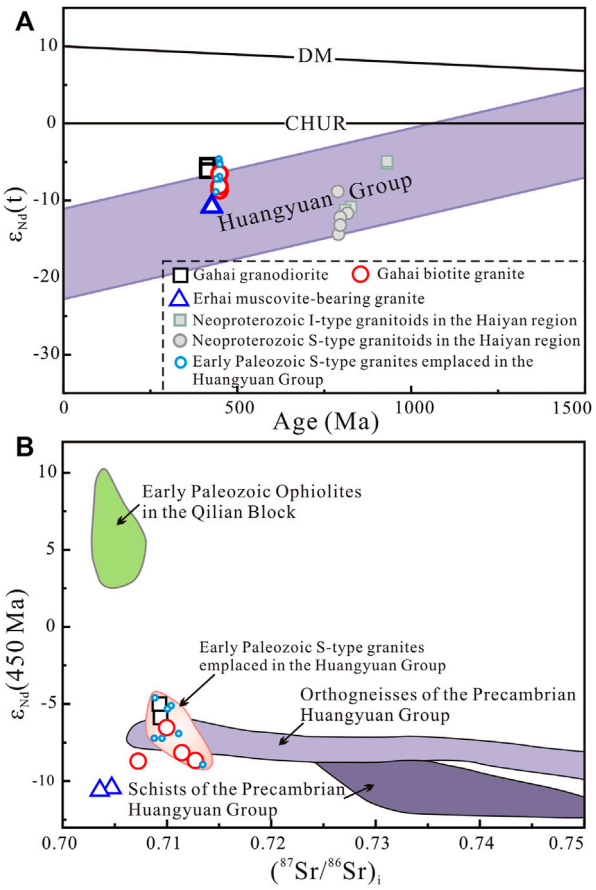


FIGURE 8
**(A)** Age vs. $\varepsilon_{Nd}(t)$ values plot for samples from the Gahai and Erhai plutons; **(B)** Whole-rock $\varepsilon_{Nd}$ (t = 450 Ma) vs. $(^{87}Sr/^{86}Sr)_i$ diagram for the Gahai and Erhai plutons (after Yang et al., 2021 and reference therein). The Nd evolutionary area shown in Figure 8A for the Precambrian basement rocks of the Huangyuan Group is calculated by the data from Tung et al. (2013) and Zhang et al. (2006). The data for the Neoproterozoic and early Paleozoic granitoids in the Haiyan region are from Tung et al. (2016) and Tung et al. (2013), respectively.

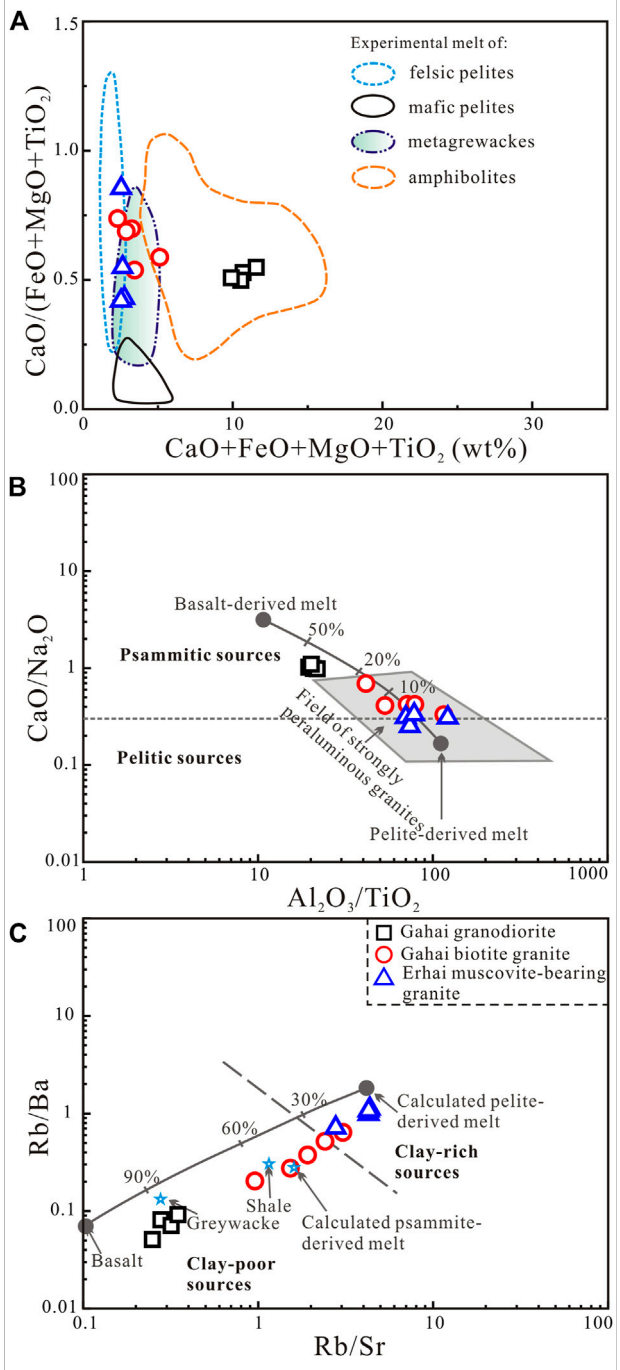


FIGURE 9
Source discrimination diagrams for the Gahai and Erhai granitoids **(A)** CaO + FeO + MgO + $TiO_2$ vs. CaO/(FeO + MgO + $TiO_2$) diagram (modified after Patiño Douce, 1999); **(B)** $Al_2O_3/TiO_2$ vs. CaO/$Na_2O$ diagram (modified after Sylvester, 1998); **(C)** Rb/Sr vs. Rb/Ba diagram (modified after Sylvester, 1998).

have significantly higher $Al_2O_3$ and normative An contents. This could be attributed to retarded crystallization of plagioclase due to high water activity. The results indicated that the investigated S- and I-type granitoids in the Qilian Block were derived from different crustal sources at different P–T conditions and were followed by variable degrees of differentiation.

Numerous studies have reported that the late Ordovician-Silurian granitoids in the Qilian Block typically show geochemical features similar to those of adakite (Tung et al., 2016; Yang et al., 2015, 2021). More recently, several granitoid intrusions from the early Devonian were identified in the Qilian Block (Figure 1), such as the Maxianshan granites (414–402 Ma, Tung et al., 2016), Subei monzogranite (ca. 413 Ma) and Sangewatang granite (ca. 417 Ma, Wang et al., 2017). These intrusions are all characterized by high HREEs and Y concentrations, and thus significantly different from adakitic rocks (Tung et al., 2016; Wang et al., 2017). These results, in combination with our new data, suggest that there does exist a

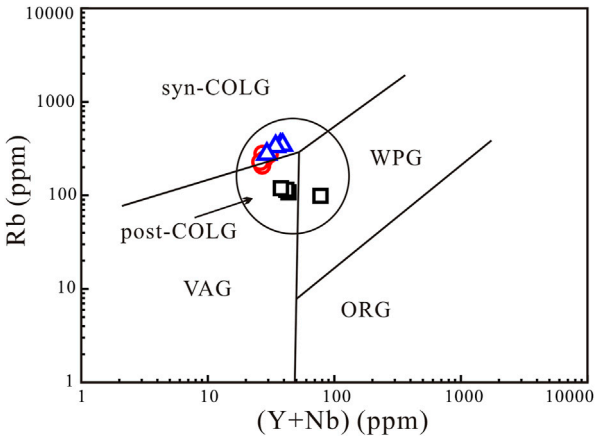


FIGURE 10
Tectonic discrimination diagrams of Pearce (1996) showing the possible tectonic setting for the Gahai and Erhai plutons. Abbreviations: WPG, within-plate granites; VAG, volcanic arc granites; syn-COLG, syn-collision granites; ORG, oceanic ridge granites; post-COLG, post-collision granites. Symbols are the same as in Figure 9.

geochemical transition from adakitic to non-adakitic magmatism at ca. 420 Ma in the Qilian Block. However, the geodynamic mechanism responsible for this change and the geological implications still remain unclear.

Despite some controversy, a growing number of researchers consider that northward subduction of the South Qilian oceanic slab beneath the Qilian Block and subsequent continental collision between the Qaidam and Qilian Blocks resulted not only in the formation of the North Qaidam ultrahigh-pressure metamorphic belt, but also in the formation of the voluminous early Paleozoic granitoids in the Qilian Block (Yang et al., 2015; Huang et al., 2016; Yang et al., 2021; Zhao et al., 2021). Based on a compilation of zircon U–Pb age data, Zhao et al. (2021) proposed that the early-middle Paleozoic granitoids in the Qilian Block primarily occurred from ca. 464 to 402 Ma, with an age peak of 455–435 Ma. The older Gahai and Erhai S-type granites show adakitic geochemical characteristics, have low MgO contents, Mg# values and relatively enriched whole-rock Sr–Nd isotopic compositions, similar to most of the ca. 464–420 Ma granitoids in the Qilian Block (Chen et al., 2008; Tung et al., 2016; Yang et al., 2021). These results indicate that the ca. 464–420 Ma granitoids in the Qilian Block occurred in a uniform tectonic setting, and were derived predominantly from partial melting of crustal materials at an over thickened lower crustal level (Yang et al., 2015; Huang et al., 2016; Xia et al., 2016; Yang et al., 2021).

S-type granitoids are generally thought to be formed by anatexis of a buried metasedimentary source in response to continental collision and intraplate orogenic activity (Sylvester, 1998; Liu et al., 2020). Post-collisional periods are commonly characterized by voluminous, mostly high-K calc-alkaline granitoid magmatism (Liégeois, 1998; Barbarin, 1999; Eyal et al., 2010). The voluminous ca. 464 to 402 Ma high-K calc-alkaline granitoids in the Qilian Block, primarily consisting of S-type and I-type granite, thus were most likely emplaced in a post-collisional setting. Moreover, both the S-type and I-type granitoids from the Gahai and Erhai plutons plot within the post-collisional granitoid field on a Y + Nb vs. Rb diagram, indicative of magmatism in a post-collisional extensional setting (Figure 10). It is worth noting that the Gahai adakitic S-type granites are nearly coeval with the Yindonggou A-type quartz monzonites (ca. 446 Ma) in the Qilian Block that also show adakitic geochemical characteristics with depletions in HREE and Y, and high La/Yb ratios (Cui et al., 2019). In addition, several bimodal intrusive rocks such as the Bamishan, Heishishan and Lumanshan plutons were recognized in the Qilian Block and emplaced between ca. 449–438 Ma (Figure 1; Guo et al., 2015; Yang et al., 2015). This indicates that both the older adakitic S-type granites and later I-type granodiorites in this study were more likely generated in a post-collisional extensional regime after slab break-off, as already proposed by Huang et al. (2016) and Yang et al. (2021, 2015). This inference is consistent with the common occurrence of granophyric textures within the Erhai and Gahai S-type granites, which has been attributed to the rapid crystallization of magma at a shallow depth (Renna et al., 2007; Zhao et al., 2016). Taken together, we propose that the over thickened lithosphere of the Qilian Block underwent lasting extensional thinning between ca. 464–402 Ma, with the geochemical transition from an adakitic to non-adakitic granitoids means significant thinning of the continental crust after ca. 420 Ma.

Based on the data presented in this paper and those from previous studies, we propose a tectonic model for the tectonic evolution of Qilian Block during late Ordovician to early Devonian time (Figure 11). After closure of the South Qilian Ocean, the northwards subducting oceanic lithosphere continued to sink, inducing continental subduction in the process. This ultimately led to the slab break-off event at ca. 464 Ma (Xia et al., 2016; Yang et al., 2021; Zhao et al., 2021), due to the contrasting behavior of the oceanic (negatively buoyant) and continental (positively buoyant) portions of the lithosphere (Davies and von Blanckenburg, 1995). At the same time, the tectonic regime in the Qilian Block switched from a collisional compressional regime to a post-collisional extensional regime (Yang et al., 2021; Zhao et al., 2021). The transfer of mantle-derived heat from mafic magmas, associated with slab break-off, resulted in anatexis of the thickened lower crust in the extensional tectonic setting. This generated the high-volume late Ordovician–Silurian adakitic granitoids typically composed of I-type and S-type granites, with minor high temperature A-type granitoids (Figure 11A; Tung et al., 2016; Cui et al., 2019). Ongoing lithospheric extension resulted in a significant thinning of the over thickened Qilian Block after ca. 420 Ma. The subsequent melting of a relatively shallow source

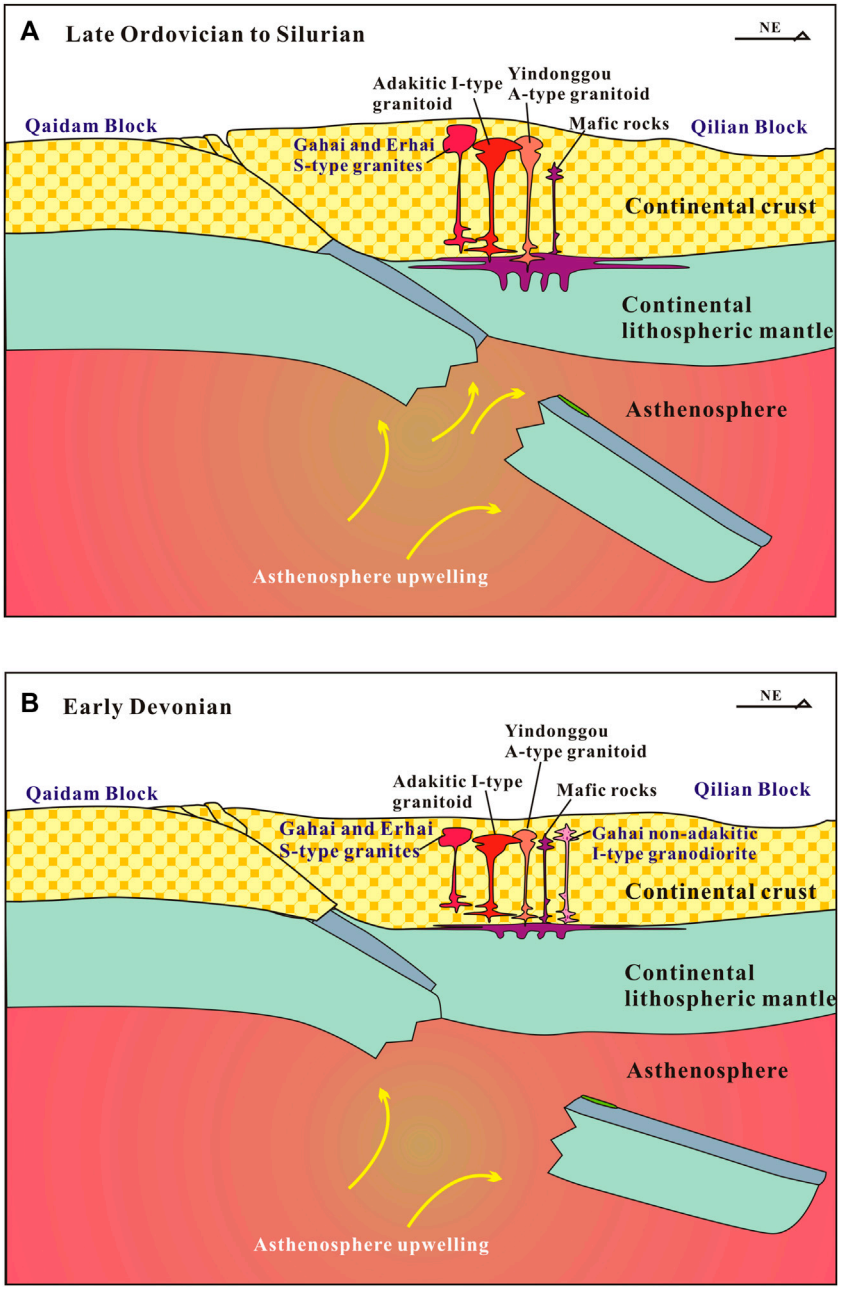


FIGURE 11
A tectonic model illustrating the tectonic evolution of the Qilian Block and the generation of the related igneous rocks during late Ordovician to early Devonian time.

produced the sparse non-adakitic I-type Gahai and Maxianshan granitoids (Figure 11B). We postulate that both the adakitic S-type granites and non-adakitic I-type granitoid from the Gahai and Erhai plutons were successively emplaced in response to a post-collisional extensional regime triggered by the break-off of a northwardly subducted South Qilian oceanic slab.

## 7 Conclusion

1) New LA–ICP–MS zircon U–Pb dating and whole-rock analysis results indicate that the Gahai biotite granite and Erhai muscovite-bearing granite are peraluminous S-type granite with adakitic geochemical characteristics and were emplaced at ca. 450 and 428 Ma, respectively, while the Gahai

granodiorites belong to non-adakitic high-K calc-alkaline, metaluminous I-type granitoid and were formed at ca. 415 Ma.

2) The older S-type granites were derived from partial melting of different sedimentary protoliths in a thickened lower crust, whereas the later I-type granodiorites were formed by partial melting of K-rich metabasaltic protoliths at shallow crustal levels, with inputs from mantle-derived melts.
3) Both types of granitoid were generated in a post-collisional extensional regime related to the break-off of the northward subducting South Qilian Ocean slab. The geochemical transition from adakitic to non-adakitic intermediate-acidic magmas indicated the ever thickened continental crust of the Qilian Block had been significantly thinned after ca. 420 Ma.

## Data availability statement

The datasets presented in this study can be found in online repositories. The names of the repository/repositories and accession number(s) can be found in the article/supplementary material.

## Author contributions

J-LZ: Investigation, Conceptualization, Methodology, Software, Data curation, Formal analysis, Writing—original draft, Writing—review and editing, Project administration, Funding acquisition. W-FC: Investigation, Formal analysis, Writing—review and editing. J-RW: Investigation, Methodology, Writing—review and editing. Q-YT: Project administration, Funding acquisition. E-TW: Investigation, Formal analysis. Y-QF: Investigation, Formal analysis.

## Funding

This study was financially supported by National Natural Science Foundation of China (Grant 41702048), Gansu Provincial Natural Science Foundation (Grant 21JR7RA503), the Fundamental Research Funds for the Central Universities (Grant lzujbky-2021-ct07) and the Second Tibetan Plateau Scientific Expedition and Research Program (Grant 2019QZKK0704).

## Acknowledgments

We acknowledge thoughtful comments and constructive suggestions by two reviewers and editor Zhuang Li, which greatly helped to improve the manuscript.

## Conflict of interest

The authors declare that the research was conducted in the absence of any commercial or financial relationships that could be construed as a potential conflict of interest.

## Publisher's note



## References

Altherr, R., Holl, A., Hegner, E., Langer, C., and Kreuzer, H. (2000). High-potassium, calcalkaline I-type plutonism in the European variscides: Northern vosges (France) and northern schwarzwald (Germany). *Lithos* 50, 51–73. doi:10.1016/s0024-4937(99)00052-3

Andersen, T. (2002). Correction of common lead in U–Pb analyses that do not report $^{204}$Pb. *Chem. Geol.* 192, 59–79. doi:10.1016/s0009-2541(02)00195-x

Barbarin, B. (1999). A review of the relationships between granitoid types, their origins and their geodynamic environments. *Lithos* 46, 605–626. doi:10.1016/s0024-4937(98)00085-1

Behrens, H., and Gaillard, F. (2006). Geochemical aspects of melts: volatiles and redox behavior. *Elements* 2, 275–280. doi:10.2113/gselements.2.5.275

Bora, S., and Kumar, S. (2015). Geochemistry of biotites and host granitoid plutons from the Proterozoic Mahakoshal Belt, central India tectonic zone: Implication for nature and tectonic setting of magmatism. *Int. Geol. Rev.* 57, 1686–1706. doi:10.1080/00206814.2015.1032372

Boynton, W. V. (1984). Chapter 3: Cosmochemistry of the rare earth elements: Meteorite studies. *Dev. Geochem.* 2, 63–114.

Chappell, B. W., and White, A. J. R. (1974). Two contrasting granite types. *Pac. Geol.* 8, 173–174.

Chen, J. L., Xu, X. Y., Zeng, Z. X., Xiao, L., Wang, H. L., Wang, Z. Q., et al. (2008). Geochemical characters and LA-ICPMS zircon U–Pb dating constraints on the petrogenesis and tectonic setting of the Shichuan intrusion, east segment of the Central Qilian, NW China. *Acta Pet. Sin.* 24 (4), 841–854. (in Chinese with English abstract).

Chung, S. L., Liu, D. Y., Ji, J. Q., Chu, M. F., Lee, H. Y., Wen, D. J., et al. (2003). Adakites from continental collision zones: Melting of thickened lower crust beneath southern tibet. *Geol.* 31, 1021. doi:10.1130/g19796.1

Corfu, F., Hanchar, J. M., Hoskin, P. W., and Kinny, P. (2003). Atlas of zircon textures. *Rev. Mineral. Geochem.* 53, 469–500. doi:10.2113/0530469

Cui, J. W., Tian, L. M., Sun, J. Y., and Yang, C. (2019). Geochronology and geochemistry of early palaeozoic intrusive rocks in the lajishan area of the eastern south Qilian belt, Tibetan plateau: implications for the tectonic evolution of South Qilian. *Geol. J.* 54, 3404–3420. doi:10.1002/gj.3327

Davies, J. H., and von Blanckenburg, F. (1995). Slab breakoff: a model of lithosphere detachment and its test in the magmatism and deformation of collisional orogens. *Earth Planet. Sci. Lett.* 129, 85–102. doi:10.1016/0012-821x(94)00237-s

Eby, G. N. (1990). The A-type granitoids: a review of their occurrence and chemical characteristics and speculations on their petrogenesis. *Lithos* 26, 115–134. doi:10.1016/0024-4937(90)90043-z

Eyal, E., Litvinovsky, B., John, B. M., Zanvilevich, A., and Katzir, Y. (2010). Origin and evolution of post–collisional magmatism: Coeval Neoproterozoic calc-alkaline

and alkaline suites of the Sinai Peninsula. *Chem. Geol.* 269, 153–179. doi:10.1016/j.chemgeo.2009.09.010

Gao, J. F., Lu, J. J., Lin, Y. P., and Pu, W. (2003). Analysis of trace elements in rock samples using HR-ICPMS. *J. Nanjing Univ. Nat. Sci.)* 39, 844–850. (in Chinese with English abstract).

Gao, X. Y., Zhao, T. P., Bao, Z. W., and Yang, A. Y. (2014). Petrogenesis of the early cretaceous intermediate and felsic intrusions at the southern margin of the north China craton: implications for crust–mantle interaction. *Lithos* 206–207, 65–78. doi:10.1016/j.lithos.2014.07.019

Guo, Z. P., Li, W. Y., Zhang, Z. W., Gao, Y. B., Zhang, J. W., and Li, K. (2015). Petrogenisis of lumanshan granites in hualong area of southern qilian mountain: constraints from geochemistry, zircon U-Pb geochronology and Hf isotope. *Geol. China* 42 (4), 864–880. (in Chinese with English abstract).

Harris, N. B. W., and Inger, S. (1992). Trace element modelling of pelite-derived granites. *Contr. Mineral. Pet.* 110, 46–56. doi:10.1007/bf00310881

Helz, R. (1976). Phase relations of basalt in their melting ranges at P $H_2O$ = 5 kb: Part 2. Melt compositions. *J. Pet.* 17, 139–193. doi:10.1093/petrology/17.2.139

Hu, F., Ducea, M. N., Liu, S., and Chapman, J. B. (2017). Quantifying crustal thickness in continental collisional belts: Global perspective and a geologic application. *Sci. Rep.* 7, 7058. doi:10.1038/s41598-017-07849-7

Huang, H., Niu, Y. L., and Mo, X. X. (2016). Syn-collisional granitoids in the qilian block on the northern Tibetan plateau: a long-lasting magmatism since continental collision through slab steepening. *Lithos* 246, 99–109. doi:10.1016/j.lithos.2015.12.018

Irvine, T. N., and Baragar, W. R. A. (1971). A guide to the chemical classification of the common volcanic rocks. *Can. J. Earth Sci.* 8, 523–548. doi:10.1139/e71-055

Jahn, B. M., Wu, F., Capdevila, R., Martineau, F., Zhao, Z., Wang, Y., et al. (2001). Highly evolved juvenile granites with tetrad REE patterns the Woduhe and Baerzhe granites from the Great Xing'an Mountains in NE China. *Lithos* 59, 171–198. doi:10.1016/s0024-4937(01)00066-4

Jiang, Y. H., and Zhu, S. Q. (2017). Petrogenesis of the late jurassic peraluminous biotite granites and muscovite-bearing granites in SE China: Geochronological, elemental and Sr–Nd–O–Hf isotopic constraints. *Contrib. Mineral. Pet.* 172 (11–12), 101. doi:10.1007/s00410-017-1422-5

Jung, S., and Pfänder, J. A. (2007). Source composition and melting temperatures of orogenic granitoids: constraints from $CaO/Na_2O$, $Al_2O_3/TiO_2$ and accessory mineral saturation thermometry. *Eur. J. Mineral.* 19, 859–870. doi:10.1127/0935-1221/2007/0019-1774

Jung, S., Mezger, K., and Hoernes, S. (1998). Petrology and geochemistry of syn- to post-collisional metaluminous A-type granites—A major and trace element and Nd–Sr–Pb–O-isotope study from the proterozoic damara belt, Namibia. *Lithos* 45 (1–4), 147–175. doi:10.1016/s0024-4937(98)00030-9

Li, J. Y., Niu, Y. L., Chen, S., Sun, W. L., Zhang, Y., Liu, Y., et al. (2017). Petrogenesis of granitoids in the eastern section of the central qilian block: evidence from geochemistry and zircon U-Pb geochronology. *Min. Pet.* 111 (1), 23–41. doi:10.1007/s00710-016-0461-3

Li, S. Z., Zhao, S. J., Liu, X., Cao, H. H., Yu, S., Li, X. Y., et al. (2018). Closure of the Proto-Tethys Ocean and early paleozoic amalgamation of microcontinental blocks in east asia. *Earth. Sci. Rev.* 186, 37–75. doi:10.1016/j.earscirev.2017.01.011

Li, Z. Y., Li, Y. L., Xiao, W. J., Zheng, J. P., and Brouwer, F. M. (2020). Geochemical and zircon U-Pb-Hf isotopic study of metasedimentary rocks from the huangyuan group of the central qilian block (NW China): Implications for paleogeographic reconstruction of rodinia. *Precambrian Res.* 351, 105947. doi:10.1016/j.precamres.2020.105947

Liégeois, J. P. (1998). Preface– some words on the post-collisional magmatism. *Lithos* 45, 15–17.

Liu, Q., Zhao, G. C., Sun, M., Han, Y. G., Eizenhöfer, P. R., Zhang, X. R., et al. (2016). Early paleozoic subduction processes of the paleo-asian ocean: insights from geochronology and geochemistry of paleozoic plutons in the Alxa terrane. *Lithos* 262, 546–560. doi:10.1016/j.lithos.2016.07.041

Liu, L., Hu, R. Z., Zhong, H., Yang, J. H., Kang, L. F., Zhang, X. C., et al. (2020). Petrogenesis of multistage s-type granites from the Malay peninsula in the southeast Asian tin belt and their relationship to tethyan evolution. *Gondwana Res.* 84, 20–37. doi:10.1016/j.gr.2020.02.013

Ma, C. Q., Yang, K. G., Ming, H. L., and Lin, G. C. (2004). The timing of tectonic transition from compression to extension in dabie orogen: evidences from mesozoic granites. *Sci. China Ser. D Earth Sci.* 47 (5), 453–462.

Maniar, P. D., and Piccoli, P. M. (1989). Tectonic discrimination of granitoids. *Geol. Soc. Am. Bull.* 101, 635–643. doi:10.1130/0016-7606(1989)101<0635:tdog>2.3.co;2

McDonough, W. F., and Sun, S. S. (1995). The composition of the Earth. *Chem. Geol.* 120, 223–253. doi:10.1016/0009-2541(94)00140-4

Middlemost, E. A. K. (1994). Naming materials in the magma/igneous rock system. *Earth. Sci. Rev.* 37, 215–224. doi:10.1016/0012-8252(94)90029-9

Miller, R. G., and O'Nions, R. K. (1985). Source of Precambrian chemical and clastic sediments. *Nature* 314, 325–330. doi:10.1038/314325a0

Patiño Douce, A. E., and Beard, J. S. (1995). Dehydration-melting of biotite gneiss and quartz amphibolite from 3 to 15 kbar. *J. Pet.* 36, 707–738. doi:10.1093/petrology/36.3.707

Patiño Douce, A. E. (1999). What do experiments tell us about the relative contributions of crust and mantle to the origin of granitic magmas. *Geol. Soc. Lond. Spec. Publ.* 168 (1), 55–75. doi:10.1144/gsl.sp.1999.168.01.05

Pearce, J. A. (1996). Sources and settings of granitic rocks. *Episodes* 19, 120–125. doi:10.18814/epiiugs/1996/v19i4/005

Peccerillo, A., and Taylor, D. R. (1976). Geochemistry of eocene calc-alkaline volcanic rocks from the Kastamonu area, Northern Turkey. *Contr. Mineral. Pet.* 58, 63–81. doi:10.1007/bf00384745

Qiu, J. T., Yu, X. Q., Santosh, M., Li, P. J., Zhang, D. H., Xiong, G. Q., et al. (2014). The late mesozoic tectonic evolution and magmatic history of west zhejiang, SE China: implications for regional metallogeny. *Int. J. Earth Sci.* 103 (3), 713–735. doi:10.1007/s00531-014-0997-6

Rapp, R. P., Shimizu, N., and Norman, M. D. (2003). Growth of early continental crust by partial melting of eclogite. *Nature* 425, 605–609. doi:10.1038/nature02031

Renna, M. R., Tribuzio, R., and Tiepolo, M. (2007). Origin and timing of the post-Variscan gabbro–granite complex of Porto (Western Corsica). *Contrib. Mineral. Pet.* 154, 493–517. doi:10.1007/s00410-007-0205-9

Richards, J. P., Spell, T., Rameh, E., Razique, A., and Fletcher, T. (2012). High Sr/Y magmas reflect arc maturity, high magmatic water content, and porphyry Cu ± Mo ± Au potential: examples from the tethyan arcs of central and eastern Iran and Western Pakistan. *Econ. Geol.* 107, 295–332. doi:10.2113/econgeo.107.2.295

Sisson, T., Ratajeski, K., Hankins, W., and Glazner, A. (2005). Voluminous granitic magmas from common basaltic sources. *Contrib. Mineral. Pet.* 148, 635–661. doi:10.1007/s00410-004-0632-9

Song, S. G., Niu, Y. L., Su, L., and Xia, X. H. (2013). Tectonics of the north qilian orogen, NW China. *Gondwana Res.* 23, 1378–1401. doi:10.1016/j.gr.2012.02.004

Song, S. G., Niu, Y. L., Su, L., Zhang, C., and Zhang, L. F. (2014). Continental orogenesis from ocean subduction, continent collision/subduction, to orogen collapse, and orogen recycling: the example of the north Qaidam UHPM belt, NW China. *Earth. Sci. Rev.* 129, 59–84. doi:10.1016/j.earscirev.2013.11.010

Sylvester, P. J. (1998). Post-collisional strongly peraluminous granites. *Lithos* 45, 29–44. doi:10.1016/s0024-4937(98)00024-3

Tung, K. A., Yang, H. Y., Liu, D. Y., Zhang, J. X., Yang, H. J., Shau, Y. H., et al. (2013). The neoproterozoic granitoids from the qilian block, NW China: evidence for a link between the qilian and south China blocks. *Precambr. Res.* 235, 163–189. doi:10.1016/j.precamres.2013.06.016

Tung, K. A., Yang, H. Y., Liu, D. Y., Zhang, J. X., Yang, H. J., Shau, Y. H., et al. (2016). Magma sources and petrogenesis of the early-middle Paleozoic backarc granitoids from the central part of the Qilian Block, NW China. *Gondwana Res.* 38, 197–219. doi:10.1016/j.gr.2015.11.012

Vanderhaeghe, O., and Teyssier, C. (2001). Crustal-scale rheological transitions during late orogenic collapse. *Tectonophysics* 335, 211–228. doi:10.1016/s0040-1951(01)00053-1

Wang, Q., Chung, S. L., Li, X. H., Wyman, D. A., Li, Z. X., Sun, W. D., et al. (2012). Crustal melting and flow beneath northern tibet: evidence from mid-miocene to quaternary strongly peraluminous rhyolites in the southern kunlun range. *J. Pet.* 53 (12), 2523–2566. doi:10.1093/petrology/egs058

Wang, C., Li, R. S., Smithies, R. H., Li, M., Peng, Y., Chen, F. N., et al. (2017). Early paleozoic felsic magmatic evolution of the Western central qilian belt, northwestern china, and constraints on convergent margin processes. *Gondwana Res.* 41, 301–324. doi:10.1016/j.gr.2015.12.009

Wang, K. X., Yu, C. D., Yan, J., Liu, X. D., Liu, W. H., Pan, J. Y., et al. (2019). Petrogenesis of early silurian granitoids in the longshoushan area and their implications for the extensional environment of the north qilian orogenic belt, China. *Lithos* 342–343, 152–174. doi:10.1016/j.lithos.2019.05.029

Watson, E. B., and Harrison, T. M. (1983). Zircon saturation revisited: temperature and composition effects in a variety of crustal magma types. *Earth Planet. Sci. Lett.* 64, 295–304. doi:10.1016/0012-821x(83)90211-x

Whalen, J. B., Currie, K. L., and Chappell, B. W. (1987). A-type granites-geochemical characteristics, discrimination and petrogenesis. *Contrib. Mineral. Pet.* 95, 407–419. doi:10.1007/bf00402202

Williams, I. S. (1998). U-Th-Pb geochronology by ion microprobe. *Rev. Econ. Geol.* 7, 1–35.

Wu, Y. B., and Zheng, Y. F. (2004). Genesis of zircon and its constraints on interpretation of U-Pb age. *Chin. Sci. Bull.* 49, 1554. doi:10.1360/04wd0130

Wu, F. Y., Sun, D. Y., Li, H. M., Jahn, B. M., and Wilde, S. (2002). A-type granites in northeastern China: age and geochemical constraints on their petrogenesis. *Chem. Geol.* 234 (1–2), 105–126.

Xia, L. Q., Li, X. M., Yu, J. Y., and Wang, G. Q. (2016). Mid–Late neoproterozoic to early paleozoic volcanism and tectonic evolution of the qilian mountain. *Geol. China* 43 (4), 1087–1138. (in Chinese with English abstract).

Xia, Y., Xu, X. S., and Liu, L. (2016a). Transition from adakitic to bimodal magmatism induced by the paleo-Pacific plate subduction and slab rollback beneath SE China: Evidence from petrogenesis and tectonic setting of the dike swarms. *Lithos* 244, 182–204. doi:10.1016/j.lithos.2015.12.006

Xiao, L., Zhang, H. F., Clemens, J. D., Wang, Q. W., Kan, Z. Z., Wang, K. M., et al. (2007). Late Triassic granitoids of the eastern margin of the Tibetan plateau: Geochronology, petrogenesis and implications for tectonic evolution. *Lithos* 96, 436–452. doi:10.1016/j.lithos.2006.11.011

Xirouchakis, D., Lindsley, D. H., and Frost, B. R. (2001). Assemblages with titanite ($CaTiOSiO_4$), Ca–Mg–Fe olivine and pyroxenes, Fe–Mg–Ti oxides, and quartz: Part II. Application. *Am. Mineral.* 86, 254–264. doi:10.2138/am-2001-2-307

Xu, H., Ma, C., Zhang, J., and Ye, K. (2013). Early cretaceous low-Mg adakitic granites from the dabie orogen, eastern China: Petrogenesis and implications for destruction of the over-thickened lower continental crust. *Gondwana Res.* 23 (1), 190–207. doi:10.1016/j.gr.2011.12.009

Yang, H., Zhang, H. F., Luo, B. J., Zhang, J., Xiong, Z. L., Guo, L., et al. (2015). Early paleozoic intrusive rocks from the eastern qilian orogen, NE Tibetan plateau: Petrogenesis and tectonic significance. *Lithos* 224, 13–31. doi:10.1016/j.lithos.2015.02.020

Yang, D. B., Xu, W. L., Zhao, G. C., Huo, T. F., Shi, J. P., Yang, H. T., et al. (2016). Tectonic implications of early cretaceous low-mg adakitic rocks generated by partial melting of thickened lower continental crust at the southern margin of the central north china craton. *Gondwana Res.* 38, 220–237. doi:10.1016/j.gr.2015.11.013

Yang, H., Zhang, H. F., Xiao, W. J., Tao, L., Gao, Z., Luo, B. J., et al. (2021). Multiple Early Paleozoic granitoids from the southeastern Qilian orogen, NW China: Magma responses to slab roll-back and break-off. *Lithos* 380–381, 105910. doi:10.1016/j.lithos.2020.105910

Yao, J., Cawood, P. A., Zhao, G. C., Han, Y. G., Xia, X. P., Liu, Q., et al. (20212021). Mariana-type ophiolites constrain the establishment of modern plate tectonic regime during Gondwana assembly. *Nat. Commun.* 12, 4189. doi:10.1038/s41467-021-24422-z

Yu, S. Y., Peng, Y. B., Zhang, J. X., Li, S. Z., Santosh, M., Li, Y. S., et al. (2021). Tectonothermal evolution of the Qilian orogenic system: Tracing the subduction, accretion and closure of the Proto-Tethys Ocean. *Earth. Sci. Rev.* 215, 103547. doi:10.1016/j.earscirev.2021.103547

Zhang, H. F., Jin, L. L., Zhang, L., Yuan, H. L., Zhou, L., and Zhang, B. R. (2006). Pb and Nd isotopic compositions of basement and granitoid in the qilianshan: constraints on tectonic affinity. *Earth Sci. J. China Univ. Geosci.* 31 (1), 57–65. (in Chinese with English abstract).

Zhang, W. X., Zhu, L. Q., Wang, H., and Wu, Y. B. (2018). Generation of post-collisional normal calc-alkaline and adakitic granites in the Tongbai Orogen, central China. *Lithos* 296, 513–531. doi:10.1016/j.lithos.2017.11.033

Zhao, L., Zhou, X. W., Zhai, M. G., Santosh, M., Ma, X. D., Shan, H. X., et al. (2014). Paleoproterozoic tectonic transition from collision to extension in the eastern Cathaysia Block, South China: Evidence from geochemistry, zircon U–Pb geochronology and Nd–Hf isotopes of a granite–charnockite suite in southwestern Zhejiang. *Lithos* 184–187, 259–280. doi:10.1016/j.lithos.2013.11.005

Zhao, J. L., Qiu, J. S., Liu, L., and Wang, R. Q. (2016). The Late Cretaceous I- and A-type granite association of southeast China: Implications for the origin and evolution of post-collisional extensional magmatism. *Lithos* 240–243, 16–33. doi:10.1016/j.lithos.2015.10.018

Zhao, J. L., Wu, B., Zhang, X., Chen, W. F., and Ma, X. X. (2021). Petrogenesis of early paleozoic adakitic granitoids in the eastern qilian block, northwest China: implications for the south Qilian ocean subduction. *Min. Pet.* 115, 687–708. doi:10.1007/s00710-021-00762-y

Zhou, C. A., Song, S. G., Allen, M. B., Wang, C., Su, L., Wang, M. J., et al. (2021). Post-collisional mafic magmatism: Insights into orogenic collapse and mantle modification from North Qaidam collisional belt, NW China. *Lithos* 398-399, 106311. doi:10.1016/j.lithos.2021.106311